

**POLITECNICO DI TORINO**

**Master's Degree in Mechanical Engineering**



**Master's Degree Thesis**

**Dynamic Structural response of  
Automotive Headlamps**

**Supervisors**

**Prof. Marco PETROLO**

**Prof. Matteo FILIPPI**

**Prof. Dario MAGLIACANO**

**Candidate**

**Venkata Sree Harsha TETTA**

**March 2025**

# Summary

The evolution of automotive lighting technology has led to the development of advanced headlamp assemblies that integrate multiple functionalities, such as main beams, Daytime Running Lights (DRL), and turn indicators, into compact units. This thesis investigates the modal behavior of automotive headlamps, focusing on the impact of temperature-dependent material properties. The study employs both commercial finite element software and the Carrera Unified Formulation (CUF) to perform comprehensive analyses at three different temperatures. Initially, modal analyses are conducted using commercial software to establish a baseline understanding of the headlamp's dynamic behavior. Subsequently, a detailed CUF-based model is developed to replicate these analyses, ensuring accurate representation of complex geometries and multi-material compositions. The CUF approach allows for a refined analysis of temperature effects on the vibrational characteristics of materials such as PMMA, PC, PC+ABS, and FR4. Comparative results highlight the differences in accuracy and computational efficiency between CUF and traditional methods, demonstrating CUF's capability to capture intricate vibrational responses under varying thermal conditions. This research contributes to optimizing headlamp designs by leveraging CUF's advanced modeling capabilities, offering recommendations for improved vibration resistance and thermal management. The study underscores the importance of integrating temperature-dependent analyses in the design process to ensure safety, reliability, and efficiency in modern automotive lighting systems.

# Acknowledgements

I want to begin by sincerely thanking my parents for their constant support throughout this journey. Their encouraging words and boundless patience have been my foundation. A special shoutout to my elder brother, who has endured all my shenanigans with admirable resilience.

I am grateful to Prof. Marco Petrolo and Prof. Matteo Filippi for allowing me the chance to collaborate with them. Their insights and expertise have been invaluable in shaping my research.

I would like to express my sincere gratitude to Prof. Dario Magliacano, whose guidance has been invaluable from the very beginning. Your continuous feedback and insightful suggestions have significantly improved the quality of my work, and your support has made this journey not only a valuable but also an enjoyable learning experience.

To all my amazing friends, thank you!



# Table of Contents

<b>List of Tables</b>	VI
<b>List of Figures</b>	VIII
<b>Acronyms</b>	XI
<b>1 Introduction</b>	1
1.1 Company Profile, Motivation, and Automotive Lighting Background	1
1.2 Problem Statement . . . . .	4
1.3 Research Objectives . . . . .	5
<b>2 Methodological Framework</b>	7
2.1 Introduction . . . . .	7
2.2 Classical Beam Models vs. Variable Kinematic Theories . . . . .	8
2.3 Governing Equations in Matrix Form . . . . .	8
2.4 Strain-Displacement and Constitutive Relations . . . . .	16
2.5 Variational Formulation and Fundamental Matrices . . . . .	16
2.6 Assembly of the Stiffness and Mass Matrices . . . . .	17
2.7 Modal Analysis . . . . .	19
<b>3 Numerical Modeling</b>	21
3.1 Geometric Simplification and Component Definition . . . . .	21
3.2 Material Properties . . . . .	23
3.3 Mesh Generation and Convergence Studies . . . . .	24
3.4 Carrera Unified Formulation (CUF) Model Setup . . . . .	28
<b>4 Results and Discussion</b>	32
4.1 Modal Analysis Process . . . . .	32
4.2 Comparison of Results . . . . .	40
4.3 Temperature-Dependent Modal Analysis Setup . . . . .	55
<b>5 Conclusions and Future Perspectives</b>	60



# List of Tables

3.1	Material properties of Polymethyl methacrylate (PMMA) lens at various temperatures. . . . .	24
3.2	Material properties of Polycarbonate+ABS (PC+ABS) housing at various temperatures. . . . .	24
3.3	Material properties of Polycarbonate (PC) bezel at various temperatures. . . . .	24
3.4	Material properties of FR-4 PCB at various temperatures. . . . .	24
4.1	Eigen Frequencies for Different Mesh Sizes (in Hz) – Ordered as 4 mm, 2 mm, and 1 mm. . . . .	33
4.2	Convergence study of modal frequencies: Relative deviations between mesh sizes. . . . .	34
4.3	Eigen frequencies (in Hz) for different mesh sizes and mesh order. . . . .	38
4.4	Calculation of Percentage Deviations and Mean Differences for Reference Mesh LE4B2_1mm mesh Compared to All Other Meshes. . . . .	41
4.5	Calculation of Percentage Deviations and Mean Differences for Reference Mesh LE4B3_1mm mesh Compared to All Other Meshes. . . . .	42
4.6	Calculation of Percentage Deviations and Mean Differences for Reference Mesh LE4B2_2mm mesh Compared to All Other Meshes. . . . .	43
4.7	Calculation of Percentage Deviations and Mean Differences for Reference Mesh LE4B3_2mm mesh Compared to All Other Meshes. . . . .	44
4.8	Calculation of Percentage Deviations and Mean Differences for Reference Mesh LE4B2_4mm mesh Compared to All Other Meshes. . . . .	45
4.9	Calculation of Percentage Deviations and Mean Differences for Reference Mesh LE4B3_4mm mesh Compared to All Other Meshes. . . . .	46
4.10	Calculation of Percentage Deviations and Mean Differences for Reference Mesh LE4LE9 B2_4mm mesh Compared to All Other Meshes. . . . .	47
4.11	Calculation of Percentage Deviations and Mean Differences for Reference Mesh LE4LE9 B3_4mm mesh Compared to All Other Meshes. . . . .	48

4.12	Calculation of Percentage Deviations and Mean Differences for Reference Mesh LE4LE9 B2B3_4mm mesh Compared to All Other Meshes. . . . .	49
4.13	Calculation of Percentage Deviations and Mean Differences for Reference Mesh Ansys_1mm mesh Compared to All Other Meshes. . .	50
4.14	Inter-Mesh Accuracy Comparison: Average Percentage Deviation of Modal Frequencies (Modes 1–10). . . . .	52
4.15	Degrees of Freedom (DOF) Percentage Matrix for Each Reference Mesh Compared to All Other Meshes. . . . .	53
4.16	Temperature-Dependent Eigen frequencies (in Hz) for the LE4 LE9-B3 Mesh. . . . .	56

# List of Figures

2.1	Geometry and adopted reference system [22]. . . . .	9
2.2	Fiber orientation angle. . . . .	12
2.3	Beam Structure [22]. . . . .	13
2.4	Plate 2D Model. . . . .	14
2.5	Cross section L-elements in natural geometry [22]. . . . .	15
2.6	Lagrange Q4 linear phase element: from material to natural ref.frame. . . . .	15
3.1	Original Headlamp Model Prior to Simplification. . . . .	22
3.2	Simplified headlamp model used for FE analysis. . . . .	22
3.3	Cross-Sectional View of the Simplified Headlamp Model with Material Annotations. . . . .	23
3.4	Cross-sectional view of the assembly highlighting the shared topology between components, ensuring continuous node equivalences at all contacting surfaces. . . . .	25
3.5	Fully hexahedral FE mesh of the model, showing (left) a Front view and (right) an isometric view with color-coded domains. . . . .	26
3.6	Meshed model with the fixed boundary conditions indicated by highlighted nodes, illustrating the fixed constraint locations applied in the analysis. . . . .	27
3.7	Linear order mesh (LE4B2), designed to maintain nearly the same number of degrees of freedom (DOFs) as the commercial FE model. . . . .	29
3.8	Linear order mesh (LE4B3), also constructed to yield a similar DOF count but employing a higher polynomial order for the in-plane expansions. . . . .	30
3.9	Variable kinematic model combining LE4 and LE9 elements with B2 and B3 expansions. This configuration aims to preserve approximate DOF equivalence while balancing accuracy across different regions. . . . .	30
4.1	Comparison of Eigen Frequencies and Mode Shapes for Varying Mesh Sizes (1 mm, 2 mm, and 4 mm) in CommercialFE Software. . . . .	33

4.2	Convergence Study: Deviation Percentage of Eigen Frequencies Across Mesh Sizes (4 mm vs 2 mm, 4 mm vs 1 mm, and 2 mm vs 1 mm) with Absolute Averages. . . . .	35
4.3	Comparison of Eigen Frequencies (in Hz) and Mode Shapes for Varying Mesh Sizes (1 mm, 2 mm, and 4 mm) of CUF models. . . .	39
4.4	Comparison of Eigen Frequencies and Mode Shapes for Linear vs Hybrid CUF models. . . . .	39
4.5	DOF vs Mesh Type. . . . .	54
4.6	Temperature-Dependent Eigenfrequencies (in Hz). . . . .	56



# Acronyms

**CUF**

Carrera Unified Formulation

**FE**

Finite Element

**FEM**

Finite Element Method

**PVD**

Principle of Virtual Displacements

**DOF**

Degrees of Freedom

**PMMA**

Polymethyl Methacrylate

**PC**

Polycarbonate

**ABS**

Acrylonitrile Butadiene Styrene

**PC+ABS**

Polycarbonate + Acrylonitrile Butadiene Styrene

**PCB**

Printed Circuit Board

**FR-4**

Flame Retardant 4

**CAD**

Computer-Aided Design

# Chapter 1

## Introduction

### 1.1 Company Profile, Motivation, and Automotive Lighting Background

Cielle-Tronics S.r.l., a successful Rivoli company near Turin, makes LED lights for cars and factories. Their key skills include electronic design and printed circuit board (PCB) development and they also have expertise in optical and mechanical design, as well as prototype creation. Cielle-Tronics possesses outstanding combined expertise in vehicular lighting innovation. This makes it an ideal industrial partner for research focused on advancing vehicular lighting technologies. Cielle-Tronics S.r.l., a homegrown mid-sized enterprise catering design innovation in automotive industry. an innovative technology company specializing in the design and development of cutting-edge electronic products that seamlessly blend a)electronic design, PCB modules, b)optical and mechanical design to develop prototype creation. At the core of this brand is a commitment to excellence in design, which serves as a key differentiator in a competitive market.

#### **Motivation**

Our collaboration with Cielle-Tronics is a direct result of their important improvements in vehicular headlamp assembly technology. Modern vehicles are increasingly incorporating compact, multi-functional lighting systems that generally merge Daytime Running Lights (DRLs), turn signals and headlamps into one unit. Light Emitting Diodes (LEDs) and laser-based solutions are now important in these assemblies. They provide benefits such as high luminous efficacy, rapid response and design flexibility [1, 2]. Our collaboration with Cielle-Tronics is resultant of

collaborative improvements, in vehicular headlamp assembly technology. Modern vehicles are indispensable of built-in compact, multi-purpose lighting systems of Daytime Running Lights (DRLs), turn signals and headlamps. For example, Light Emitting Diodes (LEDs) and laser-based solutions vehicle is product standardisation addressed imperatively for car enthusiasts worldwide. [1, 2].

Nonetheless, the design complexity of these systems derives engineering challenges. operationally, a vibration of current road conditions, as well as engine agility, can overture mechanical integrity, whilst generated heat from LEDs, diodes in compact enclosures of strong thermal management [3]. Furthermore, the important push for original brand identities has remarkably transformed headlamps from simple utility components into stylish elements specifically targeted at providing each vehicle with a special appearance. Dealing with these functional, aesthetic and durability needs points out the important importance of thorough advanced numerical modeling techniques that can effectively catch many multi-material interactions in real-world conditions.

## Background of Automotive Headlamps

The vehicular lighting landscape has been dramatically reshaped over the last twenty years, mainly due to the common integration of LED and laser technologies. Halogen as well as High-Intensity Discharge (HID) lamps were historically the most popular, but their meaningful drawbacks—like considerably lower efficiency and greatly bulkier designs—created important opportunities for newer, much more flexible alternatives. LEDs gained popularity in the mid-2000s and they quickly became favored due to their greatly better energy efficiency, outstanding mechanical strength and importantly longer lifespans [2]. They allow the possibility to be packaged in compact modules, leading to the development of highly multi-functional assemblies that integrate advanced lighting features.

Laser-based headlamps offer further improvement by providing greater luminous intensity and possibly more compact sizes [4]. Though they continue to be a remarkably special premium feature in many vehicular segments, laser lighting persists in developing exceptionally, unlocking exciting possibilities for adaptive driving beams and considerably greater illumination range.

Advanced lighting systems offer outstanding technical advantages and serve as important differentiators in vehicle design. Manufacturers use many special and impressive light signatures to significantly increase brand identity, with a growing collection of contemporary headlamps frequently incorporating detailed patterns for DRLs, turn indicators, as well as supplementary lighting elements [5]. The dual role of headlamps — combining stylish looks with better visibility — underlines their increasing importance.

Many of these significant improvements face important engineering challenges,

and they present large obstacles. The miniaturization, along with the integration of multiple functions into an importantly compact area, greatly increases thermal loads, as LEDs as well as lasers produce concentrated heat that must be efficiently dissipated to avert performance degradation [3]. Considerable vibrations from road input further complicate the situation, stressing the role and importance of mechanical stability and fatigue resistance [6]. A diverse array of materials is required. These range from many polymers for lenses, like polycarbonate or PMMA, to multiple metallic heat sinks. They must sustain their properties under wide operating temperature and ecological conditions [7]. Overall, the desire for headlamps that are smaller, smarter and more efficient increases the necessity for considerate design methods and efficient simulation practices.

Alongside the standard transition from halogen and HID lamps to LEDs and laser systems, control mechanisms that manage vehicular lighting have developed to suit the ever-changing demands. Early LED systems were predominantly static, reflecting the on/off function of their filament-based predecessors. Meaningful improvements in electronics and sensor technology have led to the development of multiple adaptive lighting systems, commonly referred to as matrix LED or pixel-level headlamp technologies [8]. These advanced systems include a large number of individually addressable LED segments, and each segment can be accurately and selectively dimmed or brightened based on instantaneous data from cameras and radar systems. These adaptive headlamps play a role in improving safety aspects by identifying all oncoming vehicles and modifying the beam pattern to effectively counteract their presence, while avoiding glare.

Additionally, creating multiple laser-based headlamps often requires several detailed optical processing methods, which may include multiple phosphor coatings to change laser light into a larger spectrum of illumination [4]. Although lasers can produce brightness and visibility across long distances, the incorporation of phosphor converters or optical waveguides complicates thermal management and heat dissipation properties. To manage these localized heat sources, advanced thermal analysis tools as well as specialized cooling systems, such as forced air vents, heat pipes, or liquid cooling loops for extreme situations [9], are necessary.

The background of vehicular headlamps includes evolving test standards in addition to reliability evaluations. Many current testing standards (e.g., ISO 16750 for road vehicles) rigorously examine the durability of electronic components against substantial shock, intense vibration, extreme temperatures and elevated humidity [10]. Diverse thermal cycling tests and several mechanical shock tests are important for forecasting real-world performance and they are particularly relevant for headlamp modules. These standards consistently change to incorporate a large variety of newer lighting technologies, which greatly raises the standard for design robustness, as well as compelling many engineers to explore a deeper depth of multi-physics simulations [11].

In the end, the relationship between cost and performance is a consistently challenging and sensitive balancing act. Many luxury cars are usually the first ones to implement the latest lighting technologies, while the large expenses for development and production are adequately covered by a higher-end market segment. As time goes on, a variety of these technologies spread to an important number of mass-market vehicles, leading to greater production and reduced unit costs. As a consequence, many vehicular OEMs pursue modular, scalable platforms that can accommodate multiple lighting features as well as fulfilling the assorted demands of global markets [12]. Grasping this evolution depicts the important importance of creating multiple headlamp assemblies that are both revolutionary and affordable.

Along with the aforementioned improvements, there has also been a greater focus on plastic component fatigue. This is particularly true because many lighting modules use polymer materials for both structural and optical functions. The VW8000 guidelines describe the steps for testing plastic materials in vehicle environments, and random vibration analysis is a required element [13]. Vibration profiles are location dependent within a vehicle. Headlamps mounted near the engine compartment or wheel arches experience higher amplitudes and frequency ranges compared to those located in more protected areas. During random vibration testing, multiple plastic materials may develop micro-cracks or suffer from damage, leading to part failure [14]. Thus, it is important to thoroughly evaluate the fatigue behavior of the polymer in dynamic load conditions to guarantee long-term reliability. Careful selection of plastic grades and design features—such as ribbing, filleting and planned reinforcement—is precise and this can greatly reduce failures in areas exposed to high cyclic stresses. Consequently, following VW8000 not only fully verifies the validity of material choices, but also guarantees that headlamp assemblies work well throughout the vehicle’s life cycle, which reduces warranty claims and safety risks.

## 1.2 Problem Statement

Modern LED headlamp systems face stringent design challenges due to compact enclosures, high-intensity light sources, and the rigorous demands of international safety and performance standards. In Europe, headlamps must comply with ECE Regulation No. 48 -[15] for vehicle lighting approval and ECE Regulation No. 112 -[16] for advanced lighting systems, which often apply to LED technology. In the United States, FMVSS No. 108 -[17] governs headlamp performance, while ISO 16750 -[10] provides guidelines for environmental and durability testing. Additionally, SAE recommendations, such as those outlined in SAE J551 -[18], inform the assessment of dynamic and fatigue behavior.

These regulatory requirements mandate comprehensive numerical modeling to

predict the dynamic response of LED headlamp components under vibrational and cyclic loading conditions. As an initial step in this analysis, modal analysis is employed to characterize the natural frequencies, mode shapes, and inherent dynamic properties critical for understanding potential fatigue issues. Building on this foundation, random vibration studies are planned to simulate real-world operational conditions, with the goal of predicting and mitigating fatigue-related failures if they are found.

This study addresses the need for a rigorous numerical framework that meets both the regulatory expectations and the technical challenges inherent to modern LED headlamp systems. By integrating modal analysis into the design process, we aim to identify critical stress points and optimize component geometries, thereby enhancing durability and ensuring compliance with standards.

### **1.3 Research Objectives**

This study addresses the challenges outlined in the previous section by presenting a detailed modal analysis of automotive headlamp assemblies, with particular emphasis on the influence of temperature-dependent material properties. The research is structured to achieve several key objectives, with each chapter contributing to the overarching goal of advancing both numerical modeling techniques and practical design strategies for automotive lighting systems.

Chapter 3 outlines the foundational steps of the analysis. The initial phase involves simplifying the actual headlamp model to meet the requirements for implementation within the Carrera Unified Formulation (CUF). Following this, a numerical model is developed for use in commercial finite element software, where modal analyses are conducted alongside a convergence study to ensure accuracy and reliability. Subsequently, a CUF-based numerical model is constructed, and modal analyses are performed using this approach as well. Consistent boundary conditions are applied across both modeling frameworks to ensure a realistic representation of real-world operating conditions.

Chapter 4 focuses on the comparative evaluation of results and methodologies. The outcomes obtained from the commercial software and CUF-based models are systematically compared, with particular attention paid to modal frequencies, mode shapes, and computational efficiency. Based on this comparison, the most effective CUF model is selected to further investigate the vibrational behavior of the headlamp assembly under three distinct temperature conditions. This analysis provides critical insights into how thermal variations influence dynamic performance, particularly at material interfaces such as lenses, housings, and printed circuit boards (PCBs).

Chapter 5 will provide the conclusion and future perspectives of the study,

summarizing the key findings and implications for both academic research and industrial practice. This chapter will highlight the potential of the Carrera Unified Formulation (CUF) in enhancing numerical modeling methodologies for analyzing the vibrational behavior of headlamp assemblies and other plastic components.

This work aims to contribute significantly to both academic research and industrial practice by enhancing numerical modeling methodologies to study headlamps under vibration and the application of CUF in the case of said component, as well as other plastic components. By bridging the gap between theoretical analysis and real-world application, this study seeks to improve not only the predictive accuracy of numerical simulations but also the overall performance and reliability of modern lighting assemblies in automotive engineering.

# Chapter 2

## Methodological Framework

### 2.1 Introduction

Over the years, classical beam theories, such as the Euler–Bernoulli and Timoshenko formulations, have been widely utilized in structural analyses due to their simplicity and computational efficiency. However, these models often fail to account for higher-order effects, including elastic bending–shear coupling, restrained torsional warping, and fully three-dimensional strain states, which become particularly significant in the analysis of thick or composite beams. To address these limitations, a range of refined theories have been developed, culminating in the introduction of the *Unified Formulation* (often referred to as **CUF**) pioneered by Carrera [19, 20].

CUF is a general hierarchical framework that systematically generates structural theories for beams, plates, and shells of variable fidelity. In recent decades, it has proven especially useful in the analysis of advanced or highly flexible structures [21]. The fundamental idea is that polynomial or other suitable expansions in the cross-section (for beams) or thickness (for plates/shells) allow one to capture complex 3D behavior in a mathematically unified manner.

Furthermore, the Finite Element Method (FEM) remains a standard computational tool in academic and industrial settings. Combining CUF with FEM helps generate low- to high-order *one-dimensional* (1D) or *two-dimensional* (2D) elements capable of capturing 3D-like accuracy at reduced computational cost, compared to a fully three-dimensional element discretization [22]. This chapter outlines the key concepts of CUF and its integration into FEM.

In particular, the current work addresses the *modal analysis* of automotive headlamp structures using both:

- A commercial solver (traditional 3D FEM).
- Carrera Unified Formulation (CUF) 1D or 2D refined models.

The goal is to verify how different kinematic expansions, shape function orders (linear vs. quadratic), and mesh resolutions (with comparable degrees of freedom) can predict the vibration characteristics of isotropic plastic components (typical in automotive headlamps).

## 2.2 Classical Beam Models vs. Variable Kinematic Theories

### Euler–Bernoulli and Timoshenko Beams

Classical beam models assume relatively slender structures:

**(Euler–Bernoulli):**

$$u_x = u_{x1}, \quad u_y = u_{y1} - x \left( \frac{\partial u_{x1}}{\partial y} \right), \quad (2.1)$$

enforcing that plane sections remain plane and perpendicular to the beam axis. Timoshenko beams relax that orthogonality assumption by allowing shear:

**(Timoshenko):**

$$u_x = u_{x1}, \quad u_y = u_{y1} + x \phi_z, \quad (2.2)$$

thus capturing shear deformation. However, neither addresses thick or composite effects comprehensively, nor do they allow for 3D warping or in-plane cross-sectional distortion [23].

### Higher-Order Refinements

To deal with torsion, warping, or in-plane distortion, additional polynomial terms can be added. For instance, a rigid rotation of the cross-section about  $y$  for torsion might be:

$$u_x = z \phi_y, \quad u_z = -x \phi_y. \quad (2.3)$$

Further expansions allow polynomial or piecewise expansions across  $(x, z)$ . The **Carrera Unified Formulation (CUF)** leverages such expansions in a systematic and hierarchical way, as discussed next [20].

## 2.3 Governing Equations in Matrix Form

### Geometrical Relations

The coordinate system adopted follows a rectangular Cartesian layout, as illustrated in Fig. 2.1, along with the geometric configuration of a beam structure. The beam's

cross-section lies on the  $xz$ -plane and is represented by  $W$ , whereas the beam extends along the  $y$ -axis within the bounds  $0 \leq y \leq L$ .

The continuous displacement field,  $u$ , of the material point can be defined as a column vector:

$$u = u(x, y, z) = \{u(x, y, z), v(x, y, z), w(x, y, z)\}^T \quad (2.4)$$

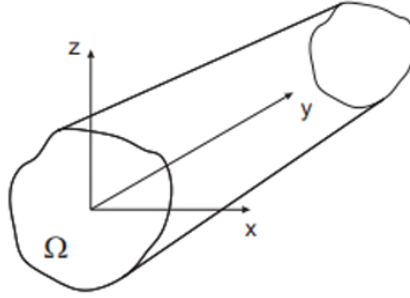


**Figure 2.1:** Geometry and adopted reference system [22].

Given that both the strain and stress tensors exhibit symmetry, they can be represented in vector notation using Voigt's representation [21]:

$$\epsilon = \{\epsilon_{xx}, \epsilon_{yy}, \epsilon_{zz}, 2\gamma_{xz}, 2\gamma_{yz}, 2\gamma_{xy}\}^T = \{\epsilon_{xx}, \epsilon_{yy}, \epsilon_{zz}, \epsilon_{xz}, \epsilon_{yz}, \epsilon_{xy}\}^T \quad (2.5)$$

$$\sigma = \{\sigma_{xx}, \sigma_{yy}, \sigma_{zz}, \sigma_{yz}, \sigma_{xz}, \sigma_{xy}\}^T \quad (2.6)$$

For accurate nonlinear analysis of flexible structures under large displacements or rotations, appropriate strain and stress definitions are required. The Lagrangian approach is typically employed for purely geometrically nonlinear analysis, with two incremental formulations: the Total Lagrangian (TL) and the Updated Lagrangian (UL) formulations [24]. In the TL formulation, strain measures reference the initial configuration, while the UL formulation describes strains relative to the deformed configuration.

To establish geometric relations, the Green-Lagrange strain tensor is considered. The strain-displacement relation is expressed as:

$$\epsilon = (b_l + b_{nl})u \quad (2.7)$$

where  $b_l$  and  $b_{nl}$  denote the linear and nonlinear derivative operators, respectively. Their explicit forms differ between 1D and 2D models [21].

The linear strain-displacement matrix for 1D models is given by:

$$b_l = \begin{bmatrix} \frac{\partial}{\partial x} & 0 & 0 \\ 0 & \frac{\partial}{\partial y} & 0 \\ 0 & 0 & \frac{\partial}{\partial z} \\ \frac{\partial}{\partial z} & 0 & \frac{\partial}{\partial x} \\ 0 & \frac{\partial}{\partial y} & \frac{\partial}{\partial x} \end{bmatrix} \quad (2.8)$$

The nonlinear strain-displacement matrix for 1D models is given by:

$$b_{nl} = \begin{bmatrix} \frac{1}{2} \frac{\partial^2}{\partial x^2} & 0 & 0 \\ 0 & \frac{1}{2} \frac{\partial^2}{\partial y^2} & 0 \\ 0 & 0 & \frac{1}{2} \frac{\partial^2}{\partial z^2} \\ \frac{\partial}{\partial x} \frac{\partial}{\partial z} & 0 & \frac{\partial}{\partial x} \frac{\partial}{\partial z} \\ 0 & \frac{\partial}{\partial y} \frac{\partial}{\partial z} & \frac{\partial}{\partial y} \frac{\partial}{\partial z} \\ \frac{\partial}{\partial x} \frac{\partial}{\partial y} & \frac{\partial}{\partial x} \frac{\partial}{\partial y} & 0 \end{bmatrix} \quad (2.9)$$

## Constitutive Equation

Assuming linear elastic materials, the constitutive equation in Voigt notation is given by:

$$\sigma = C\epsilon \quad (2.10)$$

where  $C$  represents the symmetric elasticity tensor:

$$C = \begin{bmatrix} C_{11} & C_{12} & C_{13} & C_{14} & C_{15} & C_{16} \\ C_{12} & C_{22} & C_{23} & C_{24} & C_{25} & C_{26} \\ C_{13} & C_{23} & C_{33} & C_{34} & C_{35} & C_{36} \\ C_{14} & C_{24} & C_{34} & C_{44} & C_{45} & C_{46} \\ C_{15} & C_{25} & C_{35} & C_{45} & C_{55} & C_{56} \\ C_{16} & C_{26} & C_{36} & C_{46} & C_{56} & C_{66} \end{bmatrix} \quad (2.11)$$

For isotropic materials, the elasticity tensor components are expressed in terms of Lamé parameters ( $\lambda$ ,  $G$ ), Young's modulus ( $E$ ), and Poisson's ratio ( $\nu$ ):

$$C_{11} = C_{22} = C_{33} = 2G + \lambda, \quad (2.12)$$

$$C_{12} = C_{13} = C_{23} = \lambda, \quad (2.13)$$

$$C_{44} = C_{55} = C_{66} = G. \quad (2.14)$$

The Lamé parameters  $G$  and  $\lambda$  are defined as:

$$G = \frac{E}{2(1 + \nu)}, \quad (2.15)$$

$$\lambda = \frac{\nu E}{(1 + \nu)(1 - 2\nu)}. \quad (2.16)$$

For completeness, the elasticity tensor for orthotropic materials (with a primary direction) is presented. The properties of the material in the transverse direction differ from those in the primary direction; thus, additional Young's moduli and coefficients must be defined for each direction. The elasticity tensor for orthotropic materials can be expressed as:

$$\mathbf{C} = \begin{bmatrix} C_{11} & C_{12} & C_{13} & 0 & 0 & 0 \\ C_{12} & C_{22} & C_{23} & 0 & 0 & 0 \\ C_{13} & C_{23} & C_{33} & 0 & 0 & 0 \\ 0 & 0 & 0 & C_{44} & 0 & 0 \\ 0 & 0 & 0 & 0 & C_{55} & 0 \\ 0 & 0 & 0 & 0 & 0 & C_{66} \end{bmatrix}, \quad (2.17)$$

where the components  $C_{ij}$  depend on the directional elastic properties of the orthotropic material. These include:

$$C_{ij} = C_{ij}(E_1, E_2, E_3, G_{23}, G_{13}, G_{12}, \nu_{23}, \nu_{13}, \nu_{12}) \quad (2.18)$$

- $E_1, E_2,$  and  $E_3$ : Young's moduli in the principal material directions,
- $\nu_{12}, \nu_{13}, \nu_{23}$ : Poisson's ratios for deformation coupling,
- $G_{12}, G_{13}, G_{23}$ : Shear moduli in the respective planes.

The coefficients  $C_{ij}$  depend on Young's and Poisson's moduli, as well as on the fiber orientation angle  $\theta$ , which is graphically defined in Fig. 2.2, where 1, 2, and 3 represent the axes of the material [21].

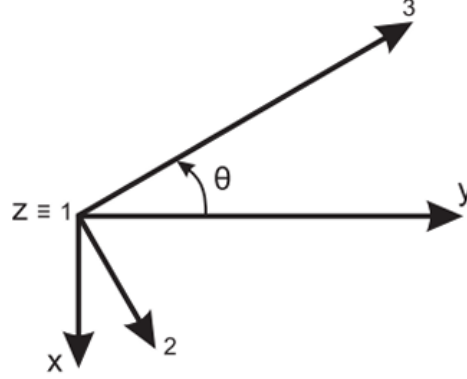


**Figure 2.2:** Fiber orientation angle.

The relationships between the components of the elasticity tensor for orthotropic materials can be further derived from these parameters.

The global material matrix  $Q$  in the transformed coordinate system is given by:

$$Q = T^T C T \quad (2.19)$$

where the transformation matrix  $T$  is defined as:

$$T = \begin{bmatrix} \cos^2 \theta & \sin^2 \theta & 0 & 0 & 0 & -\sin 2\theta \\ \sin^2 \theta & \cos^2 \theta & 0 & 0 & 0 & \sin 2\theta \\ 0 & 0 & 1 & 0 & 0 & 0 \\ 0 & 0 & 0 & \cos \theta & \sin \theta & 0 \\ 0 & 0 & 0 & -\sin \theta & \cos \theta & 0 \\ \sin \theta \cos \theta & -\sin \theta \cos \theta & 0 & 0 & 0 & \cos 2\theta \end{bmatrix} \quad (2.20)$$

Applying this transformation, Hooke's law in the global reference frame becomes:

$$\sigma = Q\epsilon \quad (2.21)$$

Applying this transformation, Hooke's law in the global reference frame becomes:

$$\sigma = Q\epsilon \quad (2.22)$$

In the interest of brevity, the expressions for the components of the matrix  $Q$  are not reported here, but can be referred to in [21, 22]. Furthermore, it should be noted that models with constant and linear distributions of the in-plane displacement

components  $u_x$  and  $u_z$ , require modified material coefficients to overcome Poisson locking [25].

### Beam 1D CUF-FEM Finite Element

Consider a beam and plate model within a Cartesian coordinate system  $(x, y, z)$ . The 1D CUF models are particularly suitable for elongated structures, such as beams, where the characteristic length significantly exceeds the cross-sectional dimensions. In this formulation, the primary variables of the three-dimensional displacement field are discretized along the longitudinal axis using a traditional finite element method (FEM), which is then used to interpolate the nodal displacement components of the cross-section [26].

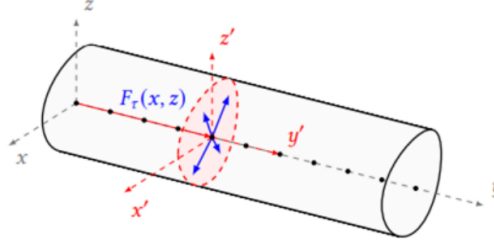


Figure 2.3: Beam Structure [22].

The derivation of the theoretical formulation remains independent of the cross-section or thickness choice. If  $y$  denotes the beam axis, and  $(x', z')$  represents the reference plane for the cross-section, the three-dimensional stationary displacement field at any arbitrary point within the structural domain is given by:

$$u(x, y, z) = F_\tau(x, z)u_\tau(y) = F_\tau(x, z)N_i(y)q_{ri}, \quad \tau = 1, 2, \dots, K \quad (2.23)$$

where  $F_\tau(x, z)$  are the cross-sectional expansion functions,  $K$  denotes the expansion order in the thickness direction, and  $q_{ri}$  represents the nodal discrete displacements. The functions  $N_i(y)$  are the standard 1D FEM shape functions used for approximating displacements along the beam axis.

### Plate 2D CUF-FEM Finite Element

For structures where the thickness is significantly smaller than the other dimensions, 2D CUF models are adopted. The displacement field is expanded using functions

approximating the displacement along the plate thickness. If  $z$  is the thickness direction and  $(x, y)$  defines the reference plane for the mid-surface of the plate, then:

$$u(x, y, z) = F_\tau(z)u_\tau(x, y) = F_\tau(z)N_i(x, y)q_{ri}, \quad \tau = 1, 2, \dots, K \quad (2.24)$$

where  $F_\tau(z)$  represents the thickness expansion function,  $K$  is the expansion order,  $q_{ri}$  are the nodal discrete displacements, and  $N_i(x, y)$  are standard 2D FEM shape functions [27].

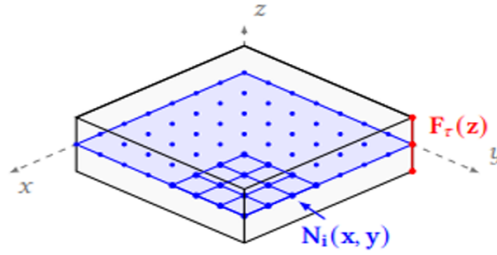


**Figure 2.4:** Plate 2D Model.

## Taylor Expansion Model

The Taylor Expansion (TE) model uses MacLaurin series, where the basis functions are polynomial terms like  $x^i z^j$ . The displacement components can be written as:

$$u_x = u_{x1} + xu_{x2} + zu_{x3}, \quad u_y = u_{y1} + xu_{y2} + zu_{y3}, \quad u_z = u_{z1} + xu_{z2} + zu_{z3}. \quad (2.25)$$

This formulation provides a hierarchical method for increasing the approximation order [20].

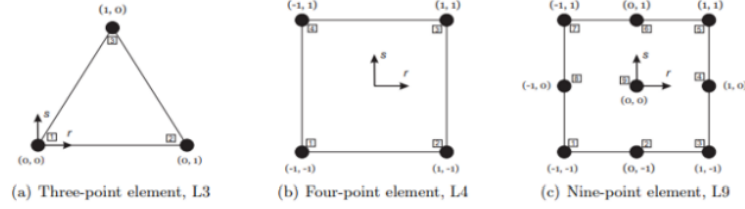


**Figure 2.5:** Cross section L-elements in natural geometry [22].

## Lagrange Expansion Model

Lagrange Expansion (LE) models use Lagrange polynomials to interpolate displacement variables over the cross-section/thickness domain. In 3D models, the displacement field is expressed using nodal displacements from the finite element mesh. Different LE orders such as Q4, Q9, and Q16 for 1D/2D elements and H8, H20, and H27 for 3D elements are implemented [28].

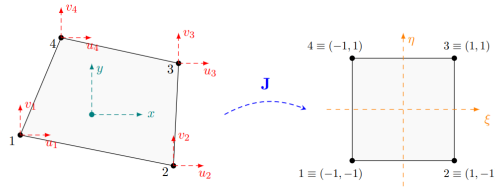


**Figure 2.6:** Lagrange Q4 linear phase element: from material to natural ref.frame.

The Lagrange polynomials in the natural reference frame are expressed as:

$$N_1(\xi, \eta) = \frac{1}{4}(1 - \xi)(1 - \eta) \quad (2.26)$$

$$N_2(\xi, \eta) = \frac{1}{4}(1 + \xi)(1 - \eta), \quad (2.27)$$

$$N_3(\xi, \eta) = \frac{1}{4}(1 + \xi)(1 + \eta) \quad (2.28)$$

$$N_4(\xi, \eta) = \frac{1}{4}(1 - \xi)(1 + \eta). \quad (2.29)$$

Once the nodal displacements are determined, the displacement field in the physical reference frame is computed using:

$$u_x = N_1 u_{x1} + N_2 u_{x2} + N_3 u_{x3} + N_4 u_{x4}. \quad (2.30)$$

$$u_y = N_1 u_{y1} + N_2 u_{y2} + N_3 u_{y3} + N_4 u_{y4}. \quad (2.31)$$

$$u_z = N_1 u_{z1} + N_2 u_{z2} + N_3 u_{z3} + N_4 u_{z4}. \quad (2.32)$$

This expansion model ensures accuracy in displacement approximations and structural analysis [21].

## 2.4 Strain-Displacement and Constitutive Relations

For small strains, the strain vector  $\boldsymbol{\epsilon}$  relates to the displacement vector  $\mathbf{u} = [u \ v \ w]^T$  via:

$$\boldsymbol{\epsilon} = B\mathbf{u}, \quad (2.33)$$

where  $B$  is the strain-displacement matrix.

Substituting the expanded displacement field (2.23) into (2.33) makes it possible to express strains in terms of the generalized unknowns  $\mathbf{u}_r(y)$  and the polynomial functions  $F_r(x, z)$ .

The constitutive relation for linear elasticity, including thermal strains, is:

$$\boldsymbol{\sigma} = C(\boldsymbol{\epsilon} - \boldsymbol{\epsilon}^T), \quad (2.34)$$

where  $C$  is the elasticity matrix and  $\boldsymbol{\epsilon}^T$  is the thermal strain vector arising from a temperature increment  $\Delta T$  [24].

## 2.5 Variational Formulation and Fundamental Matrices

The starting point for the development of the finite element model is the Principle of Virtual Displacements (PVD), which ensures that the discretized system satisfies energy balance. This principle is expressed as

$$\delta W = \int_V \delta \boldsymbol{\epsilon}^T \boldsymbol{\sigma} dV - \int_V \delta \mathbf{u}^T \mathbf{g} dV = 0, \quad (2.35)$$

where  $\delta\boldsymbol{\epsilon}$  and  $\delta\mathbf{u}$  represent the virtual strains and displacements, respectively,  $\boldsymbol{\sigma}$  is the stress vector, and  $\mathbf{g}$  is the body force vector. This formulation is in line with the approaches described in [19, 20, 21].

By substituting the constitutive relation

$$\boldsymbol{\sigma} = C (\boldsymbol{\epsilon} - \boldsymbol{\epsilon}^T), \quad (2.36)$$

and the kinematic relation

$$\boldsymbol{\epsilon} = B\mathbf{u}, \quad (2.37)$$

along with the representation of the displacement field as

$$\mathbf{u} = Nq, \quad (2.38)$$

where  $N$  comprises both the finite element shape functions and the polynomial expansions (as in the Carrera Unified Formulation, CUF), one obtains the discrete governing equation

$$Kq = f + f_T. \quad (2.39)$$

Here, the matrices and vectors are defined as follows:

$$K = \int_V B^T C B dV, \quad (2.40)$$

$$f_T = \int_V B^T C \boldsymbol{\epsilon}^T dV, \quad (2.41)$$

$$f = \int_V N^T \mathbf{g} dV. \quad (2.42)$$

For dynamic analyses, where inertia plays a critical role, the mass matrix is introduced based on the kinetic energy of the system:

$$M = \int_V N^T \rho N dV. \quad (2.43)$$

This variational framework forms the theoretical foundation for both static and dynamic analyses and has been extensively detailed in works such as [19, 21, 22].

## 2.6 Assembly of the Stiffness and Mass Matrices

Having derived the fundamental matrices from the variational formulation, the next step is to compute the element-level contributions and assemble them into global matrices.

## Assembly of the Stiffness Matrix

Within the CUF framework, the stiffness contribution for a single element is computed by evaluating its fundamental nucleus:

$$K^{\tau sij} = \int_{\Omega_e} B^{sjT} C B^{\tau i} dV, \quad (2.44)$$

where:

- $B^{\tau i}$  is the strain-displacement matrix associated with node  $i$  and polynomial expansion order  $\tau$ ,
- $C$  is the constitutive matrix,
- Indices  $\tau$  and  $s$  (ranging from 1 to  $M$ ) reflect the orders of the CUF polynomial expansion,
- Indices  $i$  and  $j$  (ranging from 1 to  $N_n$ ) refer to the finite element nodal numbering.

The complete element stiffness matrix is obtained by summing over both the nodal indices and the polynomial expansion indices. Once computed for all elements, the local stiffness matrices are assembled into the global stiffness matrix by mapping each element's contributions according to the connectivity of the mesh. Standard finite element assembly techniques, as outlined in [29], ensure that the resulting system satisfies the continuity and equilibrium conditions across element boundaries.

## Assembly of the Mass Matrix

Analogously, the element-level mass matrix is derived from the kinetic energy expression:

$$T = \frac{1}{2} \int_{\Omega} \dot{\mathbf{u}}^T \rho \dot{\mathbf{u}} dV. \quad (2.45)$$

Substituting the CUF-based approximation for the displacement field (and its time derivative) leads to the definition of the mass matrix's fundamental nucleus:

$$M^{\tau sij} = \int_{\Omega_e} N^{sjT} \rho N^{\tau i} dV, \quad (2.46)$$

where  $N^{\tau i}$  denotes the interpolation function associated with node  $i$  and expansion order  $\tau$ . Similar to the stiffness matrix, the indices span the polynomial expansion orders and the finite element nodal numbering. The element-level mass matrices are then assembled into a global mass matrix, ensuring consistency across the discretized domain.

## Numerical Integration and Efficiency Considerations

In practice, the integrals defining both the stiffness (2.44) and mass (2.46) matrices are evaluated numerically, often using Gauss-Legendre quadrature. The choice of an efficient quadrature rule is critical, especially when employing higher-order polynomial expansions inherent to CUF, to guarantee both accuracy and computational efficiency [23, 27, 26]. This systematic assembly of the global matrices not only captures complex structural behaviors but also maintains manageable computational costs, as demonstrated in [25, 28].

## Final Discrete Equations

After assembling the global mass and stiffness matrices, the governing equation for dynamic analysis can be written in the compact form

$$\mathbf{M}\ddot{\mathbf{u}} + \mathbf{K}\mathbf{u} = \mathbf{F}, \quad (2.47)$$

where:

- $\mathbf{M}$  is the global mass matrix,
- $\mathbf{K}$  is the global stiffness matrix,
- $\mathbf{u}$  is the global displacement vector (comprising all nodal displacements and polynomial expansion coefficients),
- $\mathbf{F}$  is the global force vector (assembled from body forces and prescribed tractions).

For static analyses, the inertial term is omitted, reducing the problem to

$$\mathbf{K}\mathbf{u} = \mathbf{F}. \quad (2.48)$$

## 2.7 Modal Analysis

With the global mass and stiffness matrices at hand, the next step is to investigate the dynamic behavior of the structure through modal analysis. In the absence of external forces, the free vibration equation is given by

$$\mathbf{M}\ddot{\mathbf{q}} + \mathbf{K}\mathbf{q} = \mathbf{0}, \quad (2.49)$$

where  $\mathbf{q}$  denotes the vector of nodal displacements.

Assuming a harmonic solution of the form

$$\mathbf{q}(t) = \boldsymbol{\phi} e^{i\omega t}, \quad (2.50)$$

where  $\omega$  represents the natural frequency and  $\boldsymbol{\phi}$  the corresponding mode shape, substitution into the free vibration equation yields the generalized eigenvalue problem

$$[\mathbf{K} - \omega^2 \mathbf{M}] \boldsymbol{\phi} = \mathbf{0}. \quad (2.51)$$

Solving Eq. (2.51) provides the eigenvalues  $\omega^2$ , from which the natural frequencies are determined, and the eigenvectors  $\boldsymbol{\phi}$ , which represent the mode shapes. This modal information is fundamental to understanding the dynamic characteristics of the structure and is widely used in further analyses such as dynamic response evaluation and stability assessments [30, 24, 29].

In summary, the derivation of the variational formulation and the computation of the fundamental stiffness and mass matrices set the stage for assembling the global system. This assembly is executed through standard finite element procedures enhanced by the CUF approach, which efficiently captures higher-order effects. Finally, the modal analysis based on the assembled global matrices provides insights into the dynamic behavior of the structure, thereby linking the theoretical framework with practical applications in advanced structural analysis [19, 21, 23].

# Chapter 3

## Numerical Modeling

### Overview

The modal analysis of the automotive headlamp assembly was conducted following a structured methodological approach. Initially, the geometric model was simplified to reduce computational overhead. Subsequently, mesh convergence studies were performed to determine the optimal element size for accurate results. Modal analyses were then carried out using both commercial finite element (FE) software and a Carrera Unified Formulation (CUF) model. The FE analyses included both linear and higher-order (quadratic) elements, where feasible, to assess the impact of element choice on modal characteristics. Finally, a comparative analysis was undertaken to validate the CUF model by comparing its results with those obtained from the commercial FE software under equivalent conditions.

### 3.1 Geometric Simplification and Component Definition

The original headlamp assembly consists of four major components:

1. **Lens (PMMA)**
2. **Housing (PC+ABS)**
3. **Bezel (PC)**
4. **PCB (FR-4)**

In order to reduce computational overhead while preserving essential structural dynamics, certain non-critical features such as small fillets, decorative ribs, and mounting bosses were removed.

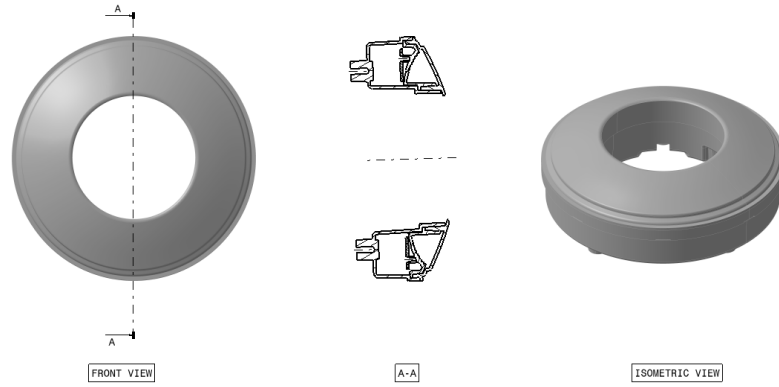


**Figure 3.1:** Original Headlamp Model Prior to Simplification.

## Simplified Model

A simplified assembly was generated by focusing on the most structurally relevant surfaces and interfaces. Fig. 3.2 illustrates the final geometry after these modifications

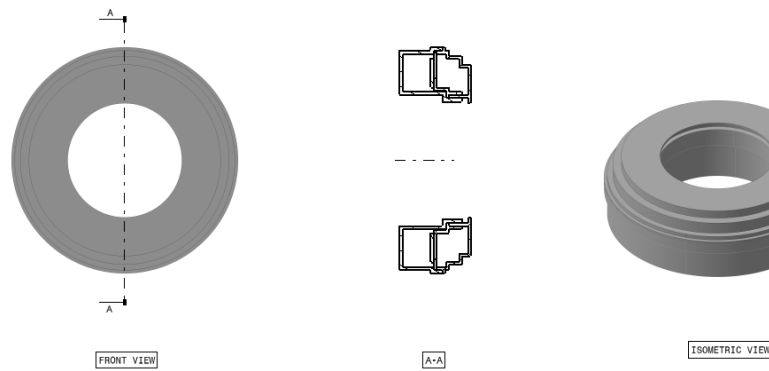


**Figure 3.2:** Simplified headlamp model used for FE analysis.

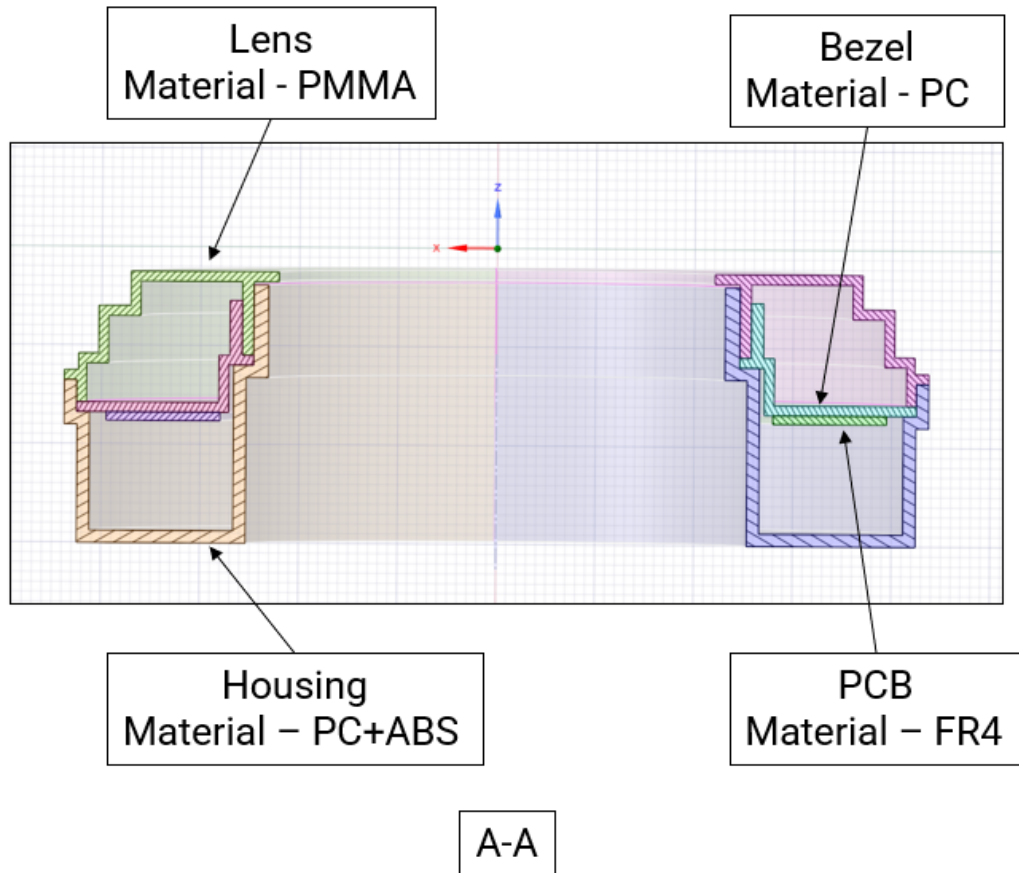


**Figure 3.3:** Cross-Sectional View of the Simplified Headlamp Model with Material Annotations.

## 3.2 Material Properties

Each headlamp component is associated with different material properties. Tab. 3.1, 3.2, 3.3 and 3.4 provides a summary of the materials and their key mechanical and thermal parameters. In instances where temperature-dependent properties are relevant, tabulated data or polynomial approximations may be used to accurately reflect variations in material stiffness.

**Table 3.1:** Material properties of Polymethyl methacrylate (PMMA) lens at various temperatures.

Temp (°C)	Young's Modulus (Pa)	Poisson's Ratio	Density (kg/m <sup>3</sup> )
-30	$3.07 \times 10^9$	0.35	1190
23	$3.30 \times 10^9$	0.35	1190
40	$3.15 \times 10^9$	0.35	1190
80	$2.82 \times 10^9$	0.35	1190

**Table 3.2:** Material properties of Polycarbonate+ABS (PC+ABS) housing at various temperatures.

Temp (°C)	Young's Modulus (Pa)	Poisson's Ratio	Density (kg/m <sup>3</sup> )
-30	$2.45 \times 10^9$	0.4	1200
23	$2.70 \times 10^9$	0.4	1200
40	$2.59 \times 10^9$	0.4	1200
80	$2.27 \times 10^9$	0.4	1200

**Table 3.3:** Material properties of Polycarbonate (PC) bezel at various temperatures.

Temp (°C)	Young's Modulus (Pa)	Poisson's Ratio	Density (kg/m <sup>3</sup> )
-30	$2.613 \times 10^9$	0.31	1200
23	$2.35 \times 10^9$	0.31	1200
40	$2.2463 \times 10^9$	0.31	1200
80	$1.942 \times 10^9$	0.31	1200

**Table 3.4:** Material properties of FR-4 PCB at various temperatures.

Temp (°C)	Young's Modulus (Pa)	Poisson's Ratio	Density (kg/m <sup>3</sup> )
-30	$1.8626 \times 10^{10}$	0.118	1901
23	$1.86 \times 10^{10}$	0.118	1900
40	$1.8591 \times 10^{10}$	0.118	1899.7
80	$1.8571 \times 10^{10}$	0.118	1898.9

### 3.3 Mesh Generation and Convergence Studies

#### Initial Mesh: Linear Elements

A commercial finite element (FE) software was employed to generate the 3D mesh for the assembly. An essential preliminary step involved carefully defining the topology

of each component so that adjoining parts would share common faces, edges, and nodes at their interfaces, as showed in fig. 3.4. This ensures the global model has continuous compatibility across contact surfaces, thereby avoiding artificial gaps or overlaps that could degrade solution accuracy. A cross-sectional view of the assembly reveals how these boundaries overlap in critical contact regions, confirming that the mesher correctly enforced node equivalences along all intersecting surfaces.

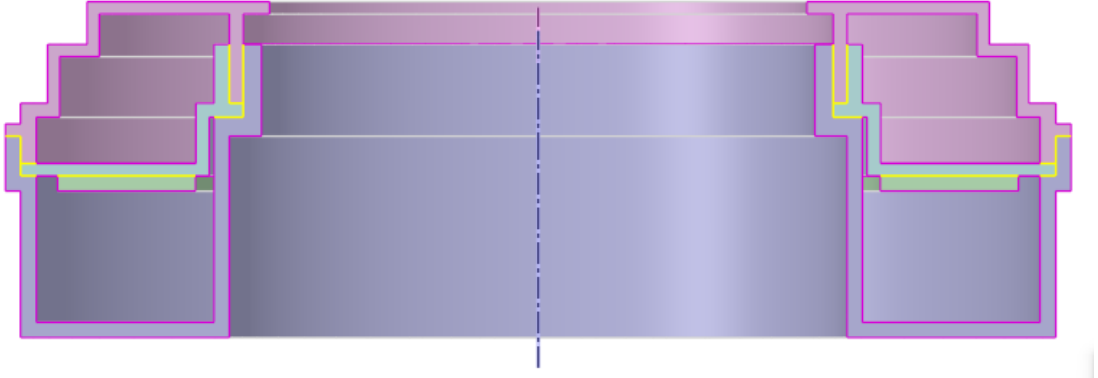


**Figure 3.4:** Cross-sectional view of the assembly highlighting the shared topology between components, ensuring continuous node equivalences at all contacting surfaces.

Once the topology was finalized, a sweep-based meshing approach was adopted to populate each part with fully hexahedral elements. In this procedure, a “sweep size” parameter governs the number of elements through the thickness of the geometry, while a “body size” specification sets the in-plane element density. Such a two-step control mechanism provides both coarse global discretization, to reduce computational cost where high resolution is unnecessary, and targeted local refinement around key features. This balance ensures that regions subject to high stress gradients or intricate geometry receive the needed element resolution, while simpler areas maintain larger, more cost-effective elements.

The exclusive use of hexahedral elements—as opposed to tetrahedral or mixed-element meshes—was motivated by several considerations. First, hexahedral meshes generally exhibit superior numerical performance and more predictable convergence behavior in both static and dynamic simulations. Second, employing fully hexahedral elements enables a direct comparison with CUF (Carrera Unified Formulation) models that rely on LE4 and LE9 element formulations, maintaining consistent geometry and mesh topology across both modeling approaches. This consistency ensures that any observed differences in subsequent analyses can be traced to the theoretical foundations of the CUF and finite element formulations, rather than to discrepancies in element shape or local refinement strategies.

Fig. 3.5 provides an overview of the final meshed assembly, revealing the overall distribution of hexahedral elements. To maintain a strictly structured hexahedral mesh throughout the main housing region, the screw housings were removed from the geometry. This omission prevents distortion of the mesh that would otherwise arise around small cylindrical features. Instead, all nodes within the radial footprint of each screw housing were fixed in place, thereby replicating the physical constraint imposed by the fastening hardware. Notably, as the mesh size varied during the convergence study, the specific nodes that fell under the screw footprints changed accordingly, ensuring each mesh iteration accurately captured the boundary condition.

As shown in Fig. 3.6 , these boundary conditions capture the functional constraints on the housing without sacrificing the element quality or uniform topology of the mesh. Coupling these targeted fixes with the locally refined sweep-based mesh ensures both computational efficiency and sufficiently accurate modeling of the part’s mechanical response.

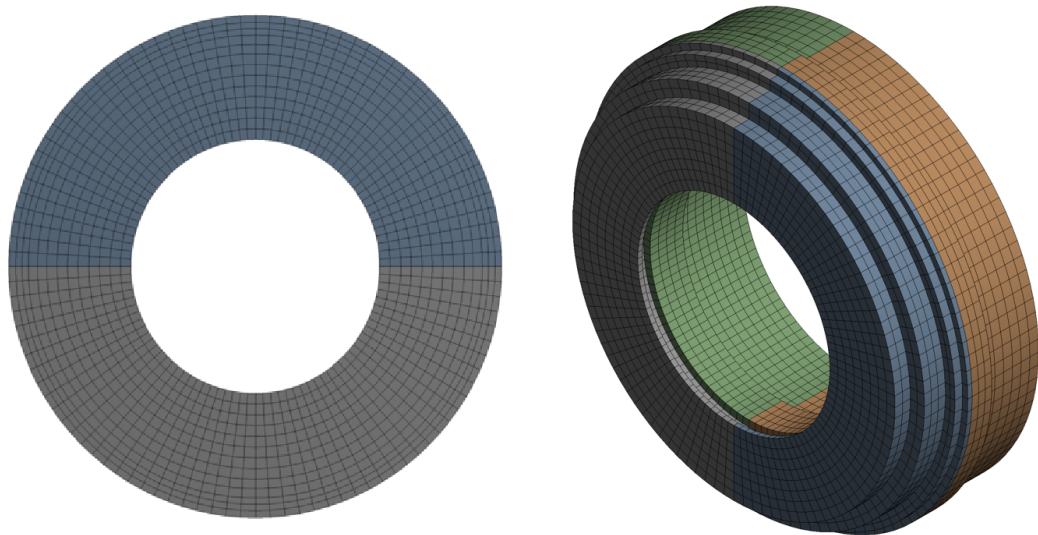


**Figure 3.5:** Fully hexahedral FE mesh of the model, showing (left) a Front view and (right) an isometric view with color-coded domains.

### Convergence Criterion

Prior to conducting the full comparison, a mesh convergence study was planned to ensure that the numerical results would not be unduly affected by the discretization. The procedure involved selecting an initial, fine-resolution mesh to capture all significant geometric details, then systematically increasing the base element size

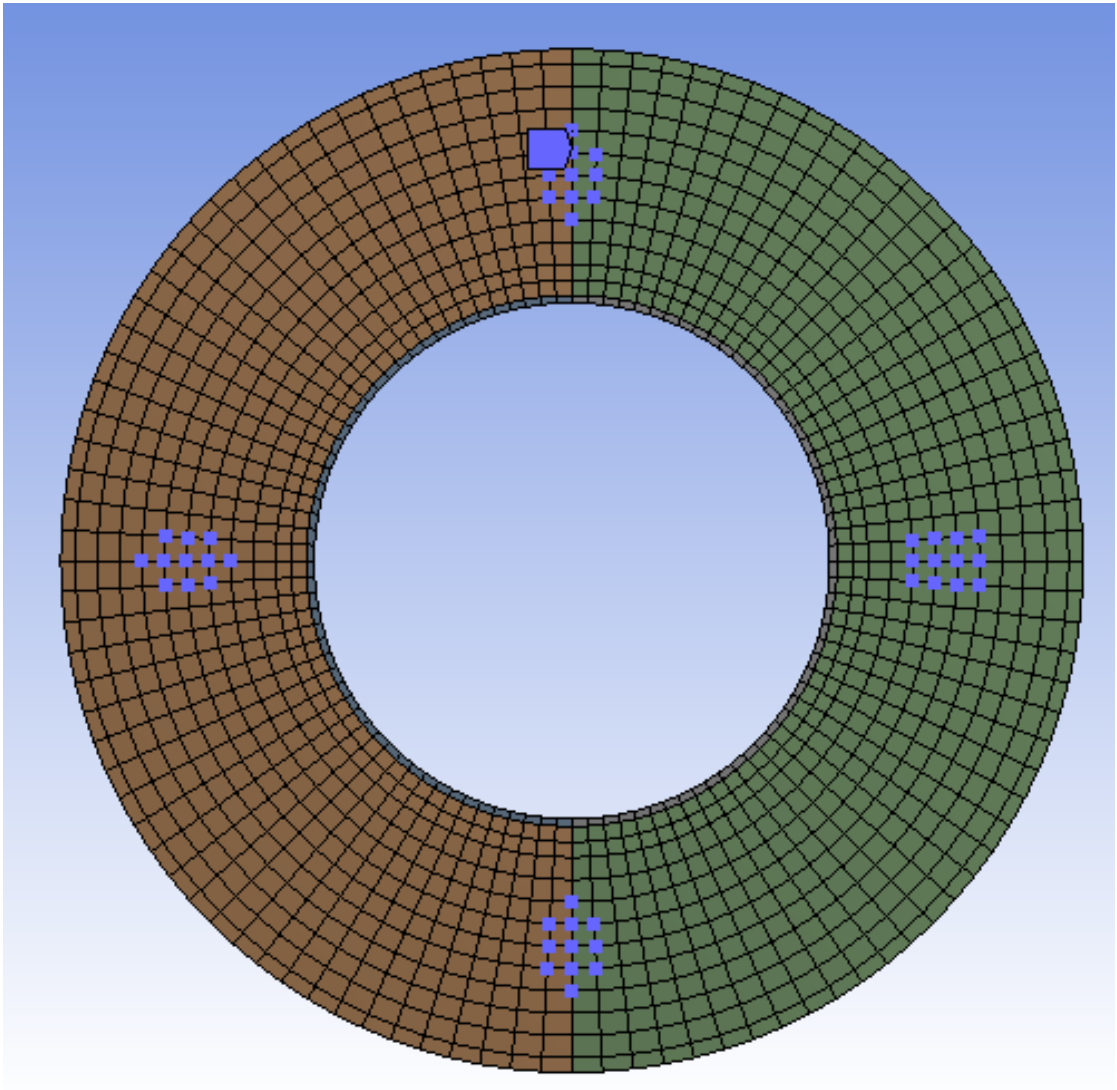


**Figure 3.6:** Meshed model with the fixed boundary conditions indicated by highlighted nodes, illustrating the fixed constraint locations applied in the analysis.

in discrete steps. At each step, key response variables—such as eigen frequencies and mode shapes—were recorded and compared to the immediately preceding, finer mesh. This comparative approach quantifies the sensitivity of the solution to mesh density, thereby guiding the choice of an optimal mesh size that strikes an acceptable balance between accuracy and computational resource demands. Attempting coarser meshes continues until either the mesher fails to generate a valid mesh or the solution changes sufficiently little to meet a predefined convergence criterion (e.g., deviations below 5%). By adopting this iterative strategy, confidence

in the reliability of the final mesh is bolstered, as it demonstrates mesh independence while minimizing unnecessary computational overhead.

## 3.4 Carrera Unified Formulation (CUF) Model Setup

### Beam-Based Approximation

To develop the Carrera Unified Formulation (CUF) model, the assembly geometry was first defined and meshed in Abaqus, from which two-dimensional (2D) cross sections were extracted at various stations along the principal axis. These cross sections were then incrementally extruded in the third dimension to build a complete beam-like representation of the structure, maintaining consistent nodal connectivity and element topology in each step. This strategy leverages the fact that the assembly, as shown in earlier figures, exhibits an elongated shape with relatively uniform or smoothly varying cross-sectional profiles, making a beam approach both computationally efficient and sufficiently accurate for capturing global bending, torsion, and axial behaviors. By isolating each 2D cross section and linking them incrementally, geometric variations—such as minor cutouts or stiffeners—are preserved without the need for a fully 3D or plate-like discretization, which could significantly increase the element count. As a result, the model strikes a balance between fidelity and performance, enabling robust stress and modal analyses while closely matching the overall geometry used in the commercial FE simulations. Moreover, limiting the formulation to beam-like kinematics allows the exploitation of higher-order expansions within CUF when needed, ensuring that any complex local phenomena can be resolved if they arise. This approach thus provides a direct, apples-to-apples comparison with the conventional FE model, clarifying how the CUF framework can replicate or potentially enhance the predictive accuracy of standard finite element solutions.

### Subdivision of Components into Multiple Bodies

In implementing the beam-like CUF model, each component of the assembly was subdivided into multiple bodies to properly account for variations in geometry and material composition. In total, 53 bodies were created: 18 corresponding to the lens, 21 to the housing, 13 to the bezel, and 1 for the PCB. These subdivisions occurred both within each cross section and along the principal axis, ensuring that every significant transition in shape or material boundary was discretized consistently. By isolating each sub-body in this manner, the incremental extrusion process could maintain structured meshing characteristics, thereby enhancing fidelity in critical

regions without unnecessarily complicating the model's geometry or increasing computational costs.

## Discretization in CUF

Three discretization strategies were considered:

1. **Linear order mesh (LE4B2):** Designed to maintain nearly the same number of degrees of freedom (DOFs) as the commercial FE model. This approach serves as a direct benchmark for comparing the results of both methods.
2. **Linear order mesh (LE4B3):** Also set up to achieve roughly the same DOF count as the commercial mesh, but with a higher polynomial order for the in-plane expansions. It aims to capture additional accuracy without a significant increase in computation.
3. **Variable kinematic model (mixed LE4 and LE9, with B2 and B3 expansions):** Incorporates both linear and higher-order elements in the cross-sectional domain, again yielding a total DOF count comparable to the commercial FE model. By mixing LE4 and LE9 elements with B2 and B3 expansions, this strategy seeks to balance accuracy and computational cost across different regions of the assembly.

Three discretization strategies were considered, each corresponding to a distinct combination of element order and polynomial expansions. Fig. 3.7, 3.8, and 3.9 illustrate the respective meshed models:

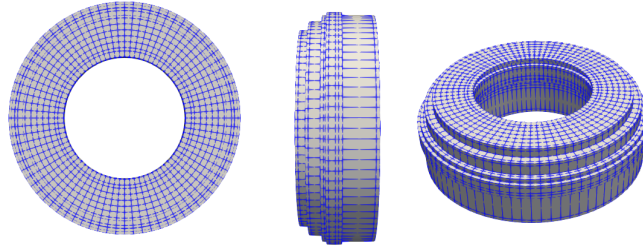


**Figure 3.7:** Linear order mesh (LE4B2), designed to maintain nearly the same number of degrees of freedom (DOFs) as the commercial FE model.

## Boundary Conditions and Modeling Assumptions

In order to maintain consistency with the commercial finite element (FE) simulations, the same boundary conditions were imposed in the CUF model. Specifically,

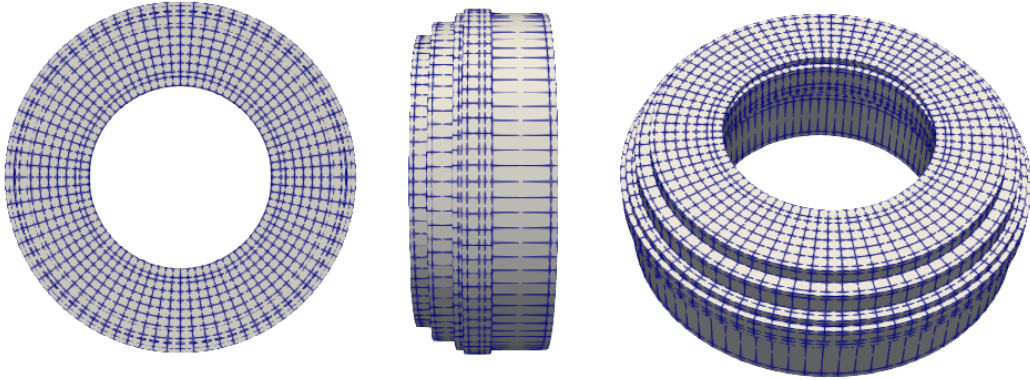


**Figure 3.8:** Linear order mesh (LE4B3), also constructed to yield a similar DOF count but employing a higher polynomial order for the in-plane expansions.

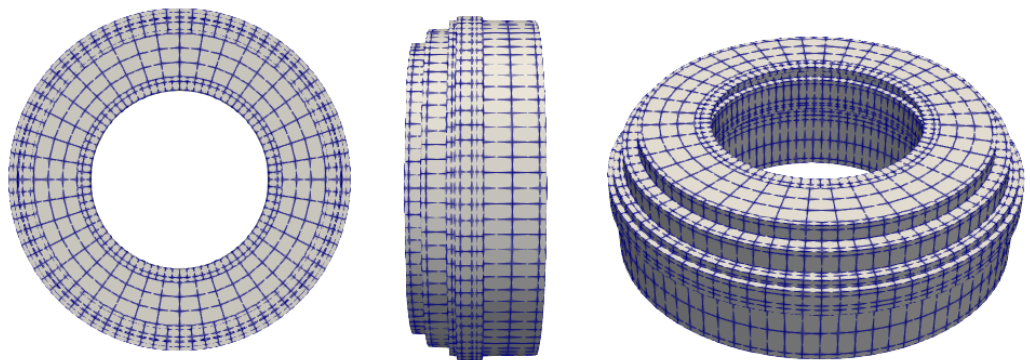


**Figure 3.9:** Variable kinematic model combining LE4 and LE9 elements with B2 and B3 expansions. This configuration aims to preserve approximate DOF equivalence while balancing accuracy across different regions.

all nodes falling under the radial footprint of the screw housings were fully constrained, effectively replicating the rigid constraint imparted by the screws in the physical assembly. This ensures that each sub-domain of the CUF model experiences the same restraining forces and displacements as its commercial FE counterpart. By matching the screw-housing constraint strategy in both models, any differences in the predicted dynamic or static responses can be attributed to the underlying theoretical formulations—rather than inconsistencies in how boundary conditions are enforced. Consequently, the CUF framework inherits the boundary environment of the commercial analysis, fostering a direct, one-to-one comparison between the two modeling approaches.

### **Thermal Integrity Assessment of the Headlight Assembly Using CUF**

To further evaluate the robustness of the CUF model, an analysis will be conducted on the variable kinematic model at  $-30^{\circ}\text{C}$ ,  $40^{\circ}\text{C}$ , and  $80^{\circ}\text{C}$ . These specific temperatures were chosen to represent extreme and operational conditions that the headlight assembly may encounter in real-world scenarios. The  $-30^{\circ}\text{C}$  case corresponds to cold-weather environments where material contraction and potential embrittlement may affect structural integrity. The  $40^{\circ}\text{C}$  condition represents an elevated ambient temperature that could be experienced in warm climates, while  $80^{\circ}\text{C}$  accounts for the thermal effects of engine heat, solar exposure, or prolonged operation. By performing simulations at these temperatures, the study aims to determine whether the headlight assembly retains its mechanical stability, modal characteristics, and overall structural integrity under varying thermal conditions. This assessment is crucial to ensuring the reliability and durability of the headlight system across a broad temperature range, validating its compliance with design requirements and industry standards.

# Chapter 4

## Results and Discussion

### 4.1 Modal Analysis Process

#### Mode Extraction

Both the commercial software FE model employs a standard eigenvalue solver and the CUF-based model employs a standard eigenvalue solver integrated within the CUF framework to extract natural frequencies and corresponding mode shapes. Furthermore, the eigen frequencies and mode shapes obtained from these models were compared using Modal Assurance Criteria (MAC) to quantitatively assess their correlation, thereby ensuring consistency and reliability in the modal analysis.

#### Modal Analysis Results and Convergence Study for the Commercial FE Model

In this section, the eigen frequency results, expressed as a function of mode number, are presented alongside the corresponding convergence study plots for the commercial FE model. The analysis was carried out using multiple mesh sizes to evaluate how the modal characteristics evolve and stabilize as the mesh is refined. In addition, the study was conducted with material properties specified for a temperature of 40°C, ensuring that the analysis reflects realistic operating conditions. The systematic investigation clearly demonstrates convergence trends in the modal results, verifying the robustness and reliability of the commercial FE model. Moreover, the detailed comparison of the results across various mesh resolutions offers valuable insights into the model's performance and its sensitivity to mesh refinement.

Tab. 4.1 presents the eigen frequencies (in Hz) obtained for three distinct mesh sizes. In this table, the data are arranged in the order of 4 mm, 2 mm, and 1 mm

to emphasize the progressive refinement in the computational model.

**Table 4.1:** Eigen Frequencies for Different Mesh Sizes (in Hz) – Ordered as 4 mm, 2 mm, and 1 mm.

Mode	4 mm	2 mm	1 mm
1	471.77	493.72	504.52
2	587.79	612.28	623.66
3	1137.3	1152.6	1160.9
4	1322.4	1319.7	1305.8
5	1404.1	1422.9	1430.1
6	1627.1	1678.2	1701.7
7	1925.5	1925.4	1919.9
8	1950.9	1948.6	1946.4
9	1953.8	1961.8	1962.7
10	2541.5	2529.8	2508.5
11	2600.6	2587.1	2553.5
12	2634.2	2607.0	2575.9
13	2960.3	2929.2	2888.8
14	3042.1	3051.2	2993.9

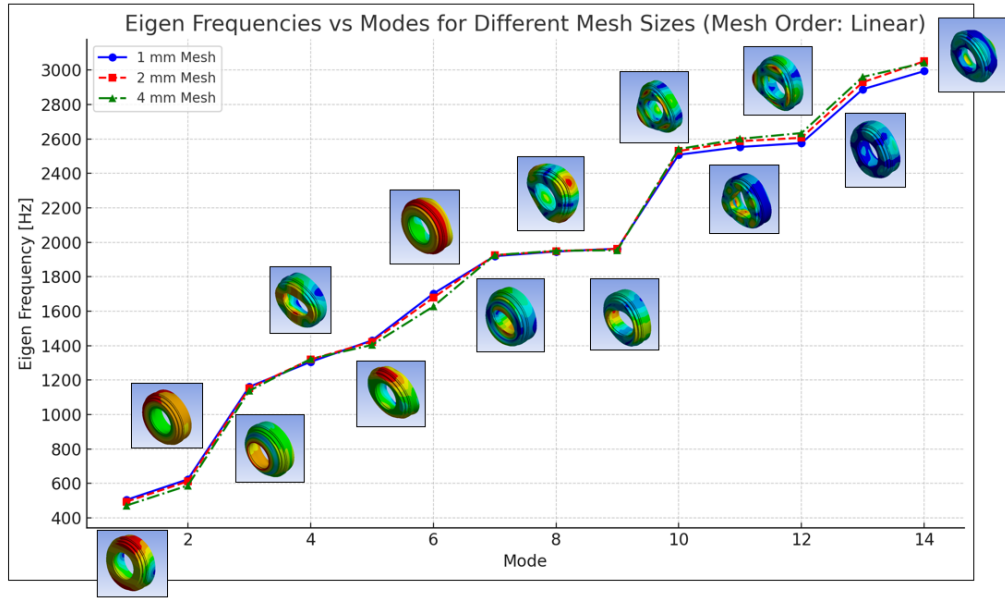


**Figure 4.1:** Comparison of Eigen Frequencies and Mode Shapes for Varying Mesh Sizes (1 mm, 2 mm, and 4 mm) in CommercialFE Software.

## Convergence Study of Modal Frequencies

In the present analysis, a staircase approach was adopted. That is, the modal analysis was first performed using a 4 mm mesh, followed by a refinement to a 2 mm mesh, and finally using a 1 mm mesh. The convergence study was carried out by comparing the results from these sequential steps. Tab. 4.2 presents the relative deviations in the eigen frequencies between the different mesh sizes. The columns labeled “4 mm vs 2 mm”, “4 mm vs 1 mm”, and “2 mm vs 1 mm” represent the percentage differences in the modal frequencies when moving from one mesh refinement level to the next, and finally, the cumulative difference between the 2 mm and 1 mm meshes.

**Table 4.2:** Convergence study of modal frequencies: Relative deviations between mesh sizes.

Mode	4 mm vs 2 mm (%)	4 mm vs 1 mm (%)	2 mm vs 1 mm (%)
1	-4.45%	-6.49%	-2.14%
2	-4.00%	-5.75%	-1.82%
3	-1.33%	-2.03%	-0.71%
4	0.20%	1.27%	1.06%
5	-1.32%	-1.82%	-0.50%
6	-3.04%	-4.38%	-1.38%
7	0.01%	0.29%	0.29%
8	0.12%	0.23%	0.11%
9	-0.41%	-0.45%	-0.05%
10	0.46%	1.32%	0.85%
11	0.52%	1.84%	1.32%
12	1.04%	2.26%	1.21%
13	1.06%	2.48%	1.40%
14	-0.30%	1.61%	1.91%

## Graphical Analysis of Modal Deviations

Fig. 4.2 illustrates the deviation percentage versus mode number for each mesh comparison. This plot, following the staircase approach, provides a clear visual representation of how the modal frequency deviations vary in the order of 4 mm vs 2 mm, 4 mm vs 1 mm, and 2 mm vs 1 mm.

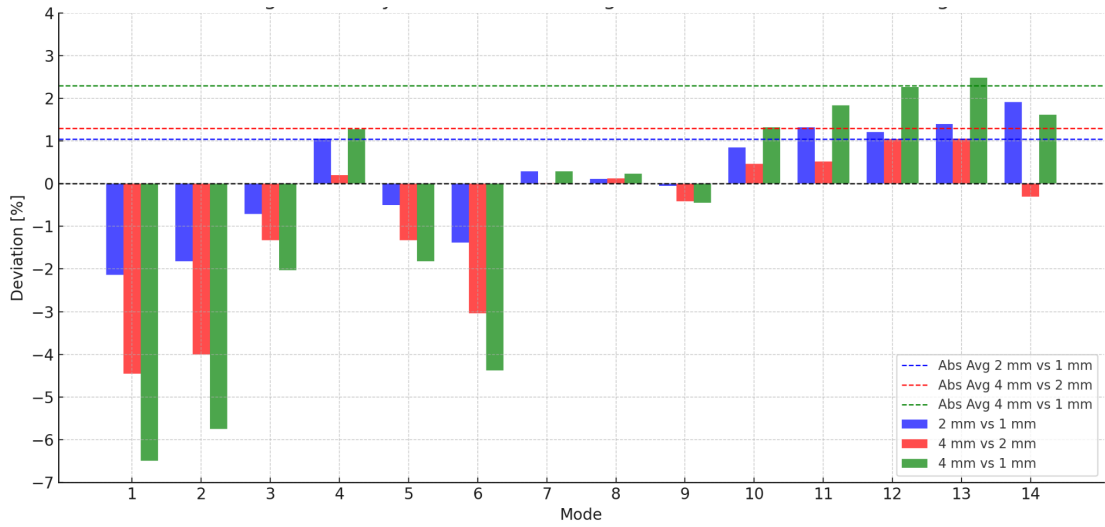


**Figure 4.2:** Convergence Study: Deviation Percentage of Eigen Frequencies Across Mesh Sizes (4 mm vs 2 mm, 4 mm vs 1 mm, and 2 mm vs 1 mm) with Absolute Averages.

## Rationale for Selecting a 1 mm Mesh Size for Comparative Study

The decision to adopt a 1 mm mesh size in this comparative study is primarily motivated by its superior convergence properties and enhanced accuracy, which ensure that the modal characteristics of the system are captured with maximum fidelity. While finer meshes typically entail increased computational costs, the benefits of higher resolution and robust convergence behavior are critical for rigorous cross-software validation. Several key considerations underscore the selection of the 1 mm mesh as the convergent choice for this investigation.

A central factor in this decision is the enhanced accuracy and reduced deviation levels achieved with the 1 mm mesh. The convergence study conducted reveals a marked decrease in relative deviations in computed eigenfrequencies as the mesh is refined. For instance, the deviation between results obtained using 2 mm and 1 mm meshes is significantly smaller than that observed between coarser discretizations, such as the comparison between 4 mm and 2 mm meshes. Specifically, for Mode 1, the relative deviation between the 2 mm and 1 mm meshes is approximately 2.14%, with similar trends observed across other modes. This reduction in deviation highlights the ability of the 1 mm mesh to provide a highly accurate representation of the system's dynamic behavior, capturing subtle modal characteristics that might otherwise be overlooked with coarser meshes.

Another important consideration is the superior convergence behavior exhibited

by the 1 mm mesh across all modes. A detailed evaluation of convergence patterns indicates that this mesh size delivers stable and reliable estimates of modal frequencies, particularly for higher modes where discrepancies between coarser meshes become increasingly pronounced. The analysis, which includes absolute averages of deviations across modes, demonstrates that further refinement beyond 1 mm yields negligible improvements. This finding confirms that the 1 mm mesh can be regarded as sufficiently converged and adequately resolved for capturing all modes of interest.

From a computational perspective, while it is acknowledged that adopting a 1 mm mesh entails higher resource demands compared to coarser alternatives such as a 4 mm mesh, this incremental cost is justified by substantial gains in accuracy and reliability. In the context of cross-software validation—where achieving high-fidelity comparisons is paramount—the increased computational expense is offset by the necessity to minimize numerical artifacts. The adoption of a 1 mm mesh thus represents an optimal balance between computational efficiency and the level of detail required for dynamic analysis.

Finally, the relevance of this resolution to cross-software comparative analysis further substantiates its selection. The eigen frequencies and mode shapes derived from the 1 mm mesh serve as a high-fidelity benchmark for comparisons with results obtained from alternative computational platforms. Since one of the primary objectives is to identify relative deviations and discern behavioral trends across different software tools, it is imperative that the reference dataset accurately reflects true physical phenomena. The enhanced resolution provided by the 1 mm mesh ensures this level of accuracy, allowing any differences observed in cross-platform analyses to be confidently attributed to methodological variations rather than inadequacies in mesh resolution.

In conclusion, the adoption of a 1 mm mesh size is driven by its ability to deliver enhanced accuracy, superior convergence behavior, and reliability while maintaining relevance for cross-software validation. This resolution strikes an optimal balance between computational cost and fidelity, ensuring that the dynamic behavior of the system is captured with maximum precision for rigorous scientific investigation.

## **Modal Analysis Results and Convergence Study for the CUF Model**

In this section, we present the modal analysis results and the corresponding convergence study for the CUF model. The approach adopted here involves a sequential refinement of the mesh, starting with a 1 mm mesh, followed by a 2 mm mesh, and finally a 4 mm mesh. For each mesh size, we initially employ first-order elements (denoted as LE4B2) to establish a baseline response. Subsequently, the analysis is extended by incorporating a higher-order kinematic formulation (LE4B3)

for the 1 mm, 2 mm, and 4 mm mesh sizes.

For the 4 mm mesh, further refinement of the modeling strategy is undertaken by developing a hybrid model that integrates higher-order mesh elements. This hybrid model, referred to as LE4LE9B2, leverages the enhanced spatial resolution provided by LE9 elements. In addition, the model is further augmented by adopting a higher-order kinematic formulation (B3) as well as by combining both B2 and B3 elements to capture complex dynamic behavior with greater fidelity.

This stepwise approach, starting from a fine mesh and progressing to coarser meshes with increasing element complexity, allows us to:

- Assess the convergence of the modal frequencies and mode shapes as a function of mesh refinement.
- Evaluate the impact of higher-order kinematics (transitioning from LE4B2 to LE4B3) on the accuracy of the dynamic response.
- Compare the performance of the standard formulation with the hybrid model (LE4LE9B2) in capturing the system's dynamic characteristics, particularly when using a combined kinematic approach (B2 & B3).

**Table 4.3:** Eigen frequencies (in Hz) for different mesh sizes and mesh order.

MODE	LE4 B2_1mm	LE4 B3_1mm	LE4 B2_2mm	LE4 B3_2mm	LE4 B2_4mm	LE4 B3_4mm	LE4 LE9 B2_4mm	LE4 LE9 B3_4mm	LE4 LE9 B2B3
1	634.20	511.00	577.11	483.01	609.96	516.19	642.72	533.83	566.28
2	810.70	642.00	740.70	612.30	786.51	657.29	824.40	674.73	718.48
3	1407.66	1164.95	1411.41	1208.01	1492.00	1290.86	1449.79	1235.18	1287.52
4	1297.50	1236.49	1327.70	1277.01	1460.50	1289.52	1319.91	1266.96	1286.20
5	1506.22	1432.29	1448.52	1392.12	1483.97	1427.05	1531.71	1464.24	1484.46
6	1682.09	1645.75	1554.63	1523.89	1599.00	1570.05	1708.90	1680.34	1694.86
7	2109.98	1925.70	2146.57	1981.82	2206.94	2039.23	2148.40	1979.27	2034.22
8	2024.49	1952.43	1991.15	1941.48	2022.70	1972.48	2050.25	1985.77	2014.49
9	2693.23	2510.46	2768.33	2582.44	2819.75	2633.04	2740.83	2570.16	2728.24
10	2777.50	2610.96	2876.55	2741.10	2913.18	2779.09	2872.55	2725.29	2772.65

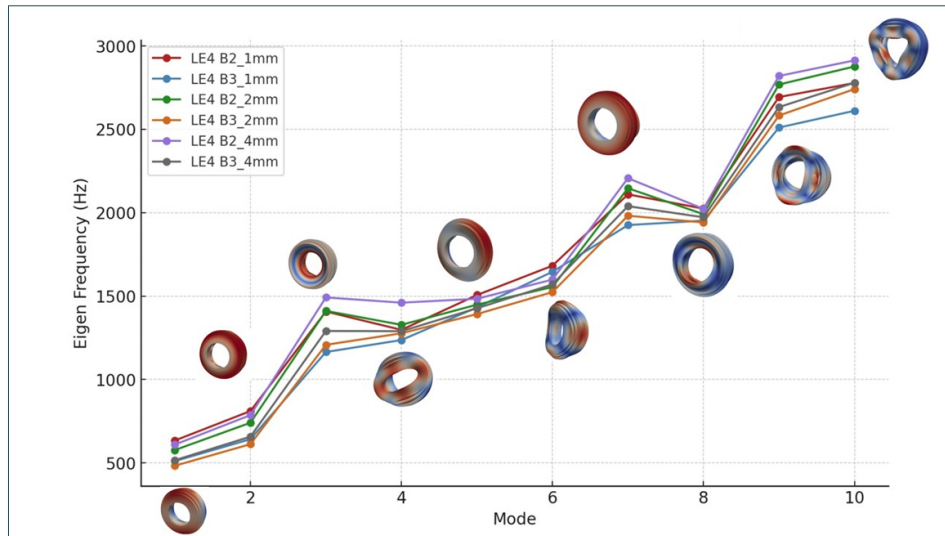


**Figure 4.3:** Comparison of Eigen Frequencies (in Hz) and Mode Shapes for Varying Mesh Sizes (1 mm, 2 mm, and 4 mm) of CUF models.

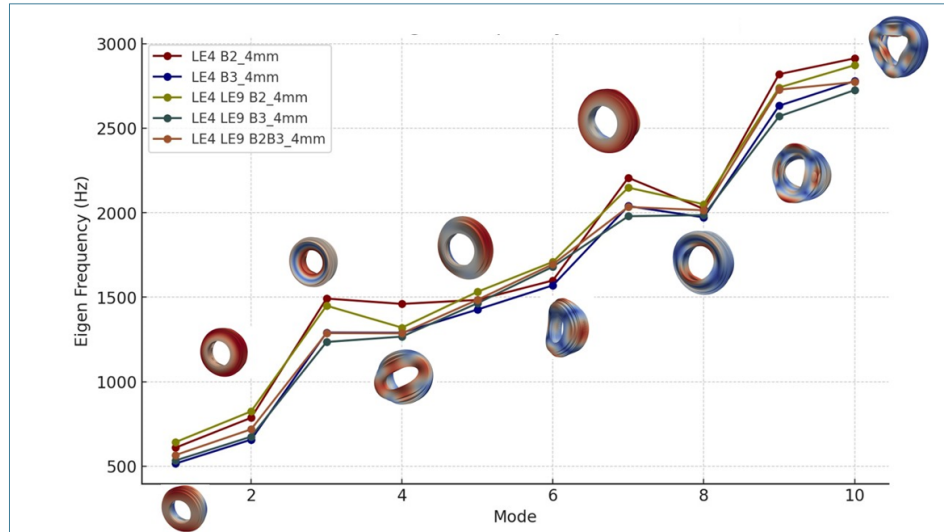


**Figure 4.4:** Comparison of Eigen Frequencies and Mode Shapes for Linear vs Hybrid CUF models.

## 4.2 Comparison of Results

### Data Extraction and Post-Processing

The post-processing organizes and compares modal results across mesh configurations. The first ten modes for each mesh are compiled into ten reference-based tables containing:

- Mode indices (1–10)
- Reference mesh frequencies
- Other nine meshes's frequencies

This structure enables mutual mesh evaluation (reference vs. target), creating a framework for subsequent calculations. The tables form the foundation for constructing accuracy (deviation matrix) and computational effort (DOF percentage matrix) comparisons.

### Calculation of Deviation Metrics

A percentage-based deviation metric compares mesh accuracy. For mode  $m$  and meshes  $(i, j)$ :

$$\text{Deviation}_{ij}(m) = \frac{\text{Value}_j(m) - \text{Value}_i(m)}{\text{Value}_i(m)} \times 100 \quad (4.1)$$

where  $\text{Value}_i(m)$  = reference mesh frequency,  $\text{Value}_j(m)$  = target mesh frequency. Calculated for all ten modes then averaged:

$$\text{AvgDeviation}_{ij} = \frac{1}{10} \sum_{m=1}^{10} \text{Deviation}_{ij}(m) \quad (4.2)$$

Positive averages indicate higher target mesh frequencies, negative values lower frequencies. Each reference table yielded nine average deviations (one per target mesh).

**Table 4.4:** Calculation of Percentage Deviations and Mean Differences for Reference Mesh LE4B2\_1mm mesh Compared to All Other Meshes.

MODE	LE4 B3_1mm	LE4 B2_2mm	LE4 B3_2mm	LE4 B2_4mm	LE4 B3_4mm	LE4 LE9 B2_4mm	LE4 LE9 B3_4mm	LE4 LE9 B2B3_4mm	Ansys_1mm
1	-19.43	-9.00	-23.84	-3.82	-18.61	1.34	-15.83	-10.71	-20.45
2	-20.81	-8.63	-24.47	-2.98	-18.92	1.69	-16.77	-11.38	-23.07
3	-17.24	0.27	-14.18	5.99	-8.30	2.99	-12.25	-8.53	-17.53
4	-4.70	2.33	-1.58	12.56	-0.62	1.73	-2.35	-0.87	-6.20
5	-4.91	-3.83	-7.58	-1.48	-5.26	1.69	-2.79	-1.44	-5.19
6	-2.16	-7.58	-9.40	-4.94	-6.66	1.59	-0.10	0.76	1.17
7	-8.73	1.73	-6.07	4.60	-3.35	1.82	-6.19	-3.59	-9.01
8	-3.56	-1.65	-4.10	-0.09	-2.57	1.27	-1.91	-0.49	-3.86
9	-6.79	2.79	-4.11	4.70	-2.23	1.77	-4.57	1.30	-6.86
10	-6.00	3.57	-1.31	4.88	0.06	3.42	-1.88	-0.17	-8.06
Average	-9.43	-2.00	-9.67	1.94	-6.65	1.93	-6.47	-3.51	-9.91

**Table 4.5:** Calculation of Percentage Deviations and Mean Differences for Reference Mesh LE4B3\_1mm mesh Compared to All Other Meshes.

MODE	LE4 B2_1mm	LE4 B2_2mm	LE4 B3_2mm	LE4 B2_4mm	LE4 B3_4mm	LE4 LE9 B2_4mm	LE4 LE9 B3_4mm	LE4 LE9 B2B3_4mm	Ansys_1mm
1	24.11	12.94	-5.48	19.37	1.02	25.78	4.47	10.82	-1.27
2	26.28	15.37	-4.63	22.51	2.38	28.41	5.10	11.91	-2.86
3	20.83	21.16	3.70	28.07	10.81	24.45	6.03	10.52	-0.35
4	4.93	7.38	3.28	18.12	4.29	6.75	2.46	4.02	-1.57
5	5.16	1.13	-2.80	3.61	-0.37	6.94	2.23	3.64	-0.30
6	2.21	-5.54	-7.40	-2.84	-4.60	3.84	2.10	2.98	3.40
7	9.57	11.47	2.91	14.60	5.90	11.56	2.78	5.64	-0.30
8	3.69	1.98	-0.56	3.60	1.03	5.01	1.71	3.18	-0.31
9	7.28	10.27	2.87	12.32	4.88	9.18	2.38	8.67	-0.08
10	6.38	10.17	4.98	11.58	6.44	10.02	4.38	6.19	-2.20
Average	11.04	8.63	-0.31	13.09	3.18	13.19	3.36	6.76	-0.58

**Table 4.6:** Calculation of Percentage Deviations and Mean Differences for Reference Mesh LE4B2\_2mm mesh Compared to All Other Meshes.

MODE	LE4 B2_1mm	LE4 B3_1mm	LE4 B3_2mm	LE4 B2_4mm	LE4 B3_4mm	LE4 LE9 B2_4mm	LE4 LE9 B3_4mm	LE4 LE9 B2B3_4mm	Ansys1mm
1	9.89	-11.46	-16.31	5.69	-10.56	11.37	-7.50	-1.88	-12.58
2	9.45	-13.33	-17.33	6.18	-11.26	11.30	-8.91	-3.00	-15.80
3	-0.27	-17.46	-14.41	5.71	-8.54	2.72	-12.49	-8.78	-17.75
4	-2.27	-6.87	-3.82	10.00	-2.88	-0.59	-4.57	-3.13	-8.33
5	3.98	-1.12	-3.89	2.45	-1.48	5.74	1.09	2.48	-1.42
6	8.20	5.86	-1.98	2.85	0.99	9.92	8.09	9.02	9.46
7	-1.70	-10.29	-7.68	2.81	-5.00	0.09	-7.79	-5.23	-10.56
8	1.67	-1.94	-2.49	1.58	-0.94	2.97	-0.27	1.17	-2.25
9	-2.71	-9.32	-6.71	1.86	-4.89	-0.99	-7.16	-1.45	-9.39
10	-3.44	-9.23	-4.71	1.27	-3.39	-0.14	-5.26	-3.61	-11.23
Average	2.28	-7.52	-7.93	4.04	-4.79	4.24	-4.48	-1.44	-7.98

**Table 4.7:** Calculation of Percentage Deviations and Mean Differences for Reference Mesh LE4B3\_2mm mesh Compared to All Other Meshes.

MODE	LE4 B2_1mm	LE4 B3_1mm	LE4 B2_2mm	LE4 B2_4mm	LE4 B3_4mm	LE4 LE9 B2_4mm	LE4 LE9 B3_4mm	LE4 LE9 B2B3_4mm	Ansys_1mm
1	31.30	5.79	19.48	26.28	6.87	33.07	10.52	17.24	4.45
2	32.40	4.85	20.97	28.45	7.35	34.64	10.20	17.34	1.86
3	16.53	-3.56	16.84	23.51	6.86	20.01	2.25	6.58	-3.90
4	1.60	-3.17	3.97	14.37	0.98	3.36	-0.79	0.72	-4.69
5	8.20	2.89	4.05	6.60	2.51	10.03	5.18	6.63	2.58
6	10.38	8.00	2.02	4.93	3.03	12.14	10.27	11.22	11.67
7	6.47	-2.83	8.31	11.36	2.90	8.41	-0.13	2.64	-3.12
8	4.28	0.56	2.56	4.18	1.60	5.60	2.28	3.76	0.25
9	4.29	-2.79	7.20	9.19	1.96	6.13	-0.48	5.05	-2.86
10	1.33	-4.75	4.94	6.28	1.39	4.80	-0.58	1.15	-6.84
Average	11.68	0.50	9.03	13.51	3.54	13.82	3.87	7.29	-0.06

**Table 4.8:** Calculation of Percentage Deviations and Mean Differences for Reference Mesh LE4B2\_4mm mesh Compared to All Other Meshes.

MODE	LE4 B2_1mm	LE4 B3_1mm	LE4 B2_2mm	LE4 B3_2mm	LE4 B3_4mm	LE4 LE9 B2_4mm	LE4 LE9 B3_4mm	LE4 LE9 B2B3_4mm	Ansys_1mm
1	3.97	-16.22	-5.39	-20.81	-15.37	5.37	-12.48	-7.16	-17.29
2	3.08	-18.37	-5.82	-22.15	-16.43	4.82	-14.21	-8.65	-20.71
3	-5.65	-21.92	-5.40	-19.03	-13.48	-2.83	-17.21	-13.71	-22.19
4	-11.16	-15.34	-9.09	-12.56	-11.71	-9.63	-13.25	-11.93	-16.67
5	1.50	-3.48	-2.39	-6.19	-3.84	3.22	-1.33	0.03	-3.77
6	5.20	2.92	-2.77	-4.70	-1.81	6.87	5.09	5.99	6.42
7	-4.39	-12.74	-2.74	-10.20	-7.60	-2.65	-10.32	-7.83	-13.01
8	0.09	-3.47	-1.56	-4.02	-2.48	1.36	-1.83	-0.41	-3.77
9	-4.49	-10.97	-1.82	-8.42	-6.62	-2.80	-8.85	-3.25	-11.04
10	-4.66	-10.37	-1.26	-5.91	-4.60	-1.39	-6.45	-4.82	-12.35
Average	-1.65	-11.00	-3.82	-11.40	-8.39	0.23	-8.08	-5.17	-11.44

**Table 4.9:** Calculation of Percentage Deviations and Mean Differences for Reference Mesh LE4B3\_4mm mesh Compared to All Other Meshes.

MODE	LE4 B2_1mm	LE4 B3_1mm	LE4 B2_2mm	LE4 B3_2mm	LE4 B2_4mm	LE4 LE9 B2_4mm	LE4 LE9 B3_4mm	LE4 LE9 B2B3_4mm	Ansys_1mm
1	22.86	-1.01	11.80	-6.43	18.17	24.51	3.42	9.70	-2.26
2	23.34	-2.33	12.69	-6.84	19.66	25.42	2.65	9.31	-5.12
3	9.05	-9.75	9.34	-6.42	15.58	12.31	-4.31	-0.26	-10.07
4	0.62	-4.11	2.96	-0.97	13.26	2.36	-1.75	-0.26	-5.62
5	5.55	0.37	1.50	-2.45	3.99	7.33	2.61	4.02	0.07
6	7.14	4.82	-0.98	-2.94	1.84	8.84	7.02	7.95	8.39
7	3.47	-5.57	5.26	-2.82	8.22	5.35	-2.94	-0.25	-5.85
8	2.64	-1.02	0.95	-1.57	2.55	3.94	0.67	2.13	-1.32
9	2.29	-4.66	5.14	-1.92	7.09	4.09	-2.39	3.62	-4.73
10	-0.06	-6.05	3.51	-1.37	4.82	3.36	-1.94	-0.23	-8.12
Average	7.69	-2.93	5.22	-3.37	9.52	9.75	0.30	3.57	-3.46

**Table 4.10:** Calculation of Percentage Deviations and Mean Differences for Reference Mesh LE4LE9 B2\_4mm mesh Compared to All Other Meshes.

MODE	LE4 B2_1mm	LE4 B3_1mm	LE4 B2_2mm	LE4 B3_2mm	LE4 B2_4mm	LE4 B3_4mm	LE4 LE9 B3_4mm	LE4 LE9 B2B3_4mm	Ausys_1mm
1	-1.33	-20.49	-10.21	-24.85	-5.10	-19.69	-16.94	-11.89	-21.50
2	-1.66	-22.13	-10.15	-25.73	-4.60	-20.27	-18.16	-12.85	-24.35
3	-2.91	-19.65	-2.65	-16.68	2.91	-10.96	-14.80	-11.19	-19.93
4	-1.70	-6.32	0.59	-3.25	10.65	-2.30	-4.01	-2.55	-7.79
5	-1.66	-6.49	-5.43	-9.11	-3.12	-6.83	-4.40	-3.08	-6.77
6	-1.57	-3.70	-9.03	-10.83	-6.43	-8.13	-1.67	-0.82	-0.42
7	-1.79	-10.37	-0.09	-7.75	2.72	-5.08	-7.87	-5.31	-10.64
8	-1.26	-4.77	-2.88	-5.31	-1.34	-3.79	-3.14	-1.74	-5.07
9	-1.74	-8.41	1.00	-5.78	2.88	-3.93	-6.23	-0.46	-8.48
10	-3.31	-9.11	0.14	-4.58	1.41	-3.25	-5.13	-3.48	-11.11
Average	-1.89	-11.14	-3.87	-11.39	0.00	-8.42	-8.24	-5.34	-11.60

**Table 4.1.1:** Calculation of Percentage Deviations and Mean Differences for Reference Mesh LE4LE9 B3\_4mm mesh Compared to All Other Meshes.

MODE	LE4 B2_1mm	LE4 B3_1mm	LE4 B2_2mm	LE4 B3_2mm	LE4 B2_4mm	LE4 B3_4mm	LE4 LE9 B2_4mm	LE4 LE9 B2B3_4mm	Absys_1mm
1	18.80	-4.28	8.11	-9.52	14.26	-3.30	20.40	6.08	-5.49
2	20.15	-4.85	9.78	-9.25	16.57	-2.58	22.18	6.48	-7.57
3	13.96	-5.69	14.27	-2.20	20.79	4.51	17.37	4.24	-6.01
4	2.41	-2.40	4.79	0.79	15.28	1.78	4.18	1.52	-3.94
5	2.87	-2.18	-1.07	-4.93	1.35	-2.54	4.61	1.38	-2.48
6	0.10	-2.06	-7.48	-9.31	-4.84	-6.56	1.70	0.86	1.27
7	6.60	-2.71	8.45	0.13	11.50	3.03	8.55	2.78	-3.00
8	1.95	-1.68	0.27	-2.23	1.86	-0.67	3.25	1.45	-1.98
9	4.79	-2.32	7.71	0.48	9.71	2.45	6.64	6.15	-2.40
10	1.92	-4.20	5.55	0.58	6.89	1.97	5.40	1.74	-6.30
Average	7.36	-3.24	5.04	-3.55	9.34	-0.19	9.43	3.27	-3.79

**Table 4.12:** Calculation of Percentage Deviations and Mean Differences for Reference Mesh LE4LE9 B2B3\_4mm mesh Compared to All Other Meshes.

MODE	LE4 B2_1mm	LE4 B3_1mm	LE4 B2_2mm	LE4 B3_2mm	LE4 B2_4mm	LE4 B3_4mm	LE4 LE9 B2_4mm	LE4 LE9 B3_4mm	Anslys_1mm
1	11.99	-9.76	1.91	-14.70	7.71	-8.85	13.50	-5.73	-10.91
2	12.84	-10.64	3.09	-14.78	9.47	-8.52	14.74	-6.09	-13.20
3	9.33	-9.52	9.62	-6.18	15.88	0.26	12.60	-4.07	-9.83
4	0.88	-3.86	3.23	-0.71	13.55	0.26	2.62	-1.50	-5.37
5	1.47	-3.51	-2.42	-6.22	-0.03	-3.87	3.18	-1.36	-3.80
6	-0.75	-2.90	-8.27	-10.09	-5.66	-7.36	0.83	-0.86	0.40
7	3.72	-5.33	5.52	-2.58	8.49	0.25	5.61	-2.70	-5.62
8	0.50	-3.08	-1.16	-3.62	0.41	-2.09	1.78	-1.43	-3.38
9	-1.28	-7.98	1.47	-5.34	3.35	-3.49	0.46	-5.79	-8.05
10	0.17	-5.83	3.75	-1.14	5.07	0.23	3.60	-1.71	-7.90
Average	3.89	-6.24	1.67	-6.54	5.82	-3.32	5.89	-3.12	-6.77

**Table 4.13:** Calculation of Percentage Deviations and Mean Differences for Reference Mesh Ansys\_1mm mesh Compared to All Other Meshes.

MODE	LE4 B2_1mm	LE4 B3_1mm	LE4 B2_2mm	LE4 B3_2mm	LE4 B2_4mm	LE4 B3_4mm	LE4 LE9 B2_4mm	LE4 LE9 B3_4mm	LE4 LE9 B2B3_4mm
1	25.70	1.28	14.39	-4.26	20.90	2.31	27.39	5.81	12.24
2	29.99	2.94	18.77	-1.82	26.11	5.39	32.19	8.19	15.20
3	21.26	0.35	21.58	4.06	28.52	11.19	24.89	6.40	10.91
4	6.61	1.59	9.09	4.92	20.00	5.95	8.45	4.10	5.68
5	5.48	0.30	1.44	-2.51	3.92	-0.07	7.26	2.54	3.95
6	-1.15	-3.29	-8.64	-10.45	-6.04	-7.74	0.42	-1.26	-0.40
7	9.90	0.30	11.81	3.23	14.95	6.22	11.90	3.09	5.95
8	4.01	0.31	2.30	-0.25	3.92	1.34	5.34	2.02	3.50
9	7.36	0.08	10.36	2.95	12.41	4.96	9.26	2.46	8.76
10	8.77	2.25	12.65	7.35	14.09	8.83	12.49	6.73	8.58
Average	11.79	0.61	9.37	0.32	13.88	3.84	13.96	4.01	7.44

## Construction of Deviation Matrix

The ten average deviations from each reference-based tables from Tab. 4.4 to Tab. 4.13 were consolidated into a single  $10 \times 10$  deviation matrix, providing a comprehensive view of all pairwise comparisons. In this matrix architecture:

- Rows correspond to reference meshes ( $i$ )
- Columns represent target meshes ( $j$ )

Diagonal entries ( $i = j$ ) inherently equal zero, as these positions compare each mesh to itself as shown in Tab. 4.14. This symmetrical structure enables rapid visual assessment of relative solution fidelity across all mesh combinations.

## Construction of the DOF Matrix

The DOF percentage matrix is constructed by comparing degrees of freedom between each target mesh and reference mesh pair. For each reference–target combination ( $i, j$ ), the percentage difference is calculated as:

$$\text{DOF}_{\text{diff}}(i, j) = \frac{\text{DOF}_j - \text{DOF}_i}{\text{DOF}_i} \times 100 \quad (4.3)$$

where  $\text{DOF}_i$  and  $\text{DOF}_j$  denote the total degrees of freedom in the reference and target meshes, respectively. The matrix structure follows:

- Rows: Reference meshes
- Columns: Target meshes

## Matrix Interpretation

Each cell contains:

- Positive values: Target mesh has more DOFs than reference
- Negative values: Target mesh has fewer DOFs
- Zero diagonals: Self-comparison yields no difference

## Practical Significance

This matrix enables rapid assessment of computational complexity across meshes, serving as a decision-making tool for balancing numerical accuracy against computational costs. Engineers can instantly identify meshes with disproportionate resource demands relative to others in the configuration set.

**Table 4.14:** Inter-Mesh Accuracy Comparison: Average Percentage Deviation of Modal Frequencies (Modes 1–10).

Reference Target	LE4 B2_1mm	LE4 B3_1mm	LE4 B2_2mm	LE4 B3_2mm	LE4 B2_4mm	LE4 B3_4mm	LE4 LE9 B2_4mm	LE4 LE9 B3_4mm	LE4 LE9 B2B3_4mm	Ansys_1mm
LE4 B2_1mm	0.00	-9.43	-2.00	-9.67	1.94	-6.65	1.93	-6.47	-3.51	-9.91
LE4 B3_1mm	11.04	0.00	8.63	-0.31	13.09	3.18	13.20	3.36	6.76	-0.58
LE4 B2_2mm	2.28	-7.51	0.00	-7.94	4.04	-4.80	4.24	-4.48	-1.44	-7.99
LE4 B3_2mm	11.69	0.49	9.04	0.00	13.52	3.55	13.82	3.87	7.29	-0.06
LE4 B2_4mm	-1.65	-11.00	-3.82	-11.40	0.00	-8.39	0.23	-8.08	-5.17	-11.43
LE4 B3_4mm	7.69	-2.33	5.22	-3.37	9.52	0.00	9.75	0.31	3.58	-3.46
LE4 LE9 B2_4mm	-1.89	-11.14	-3.87	-11.39	0.00	-8.42	0.00	-8.23	-5.34	-11.60
LE4 LE9 B3_4mm	7.36	-3.24	5.04	-3.55	9.33	-0.19	9.42	0.00	3.27	-3.79
LE4 LE9 B2B3_4mm	3.88	-6.24	1.67	-6.53	5.82	-3.32	5.89	-3.12	0.00	-6.77
Ansys_1mm	11.79	0.61	9.37	0.32	13.87	3.84	13.96	4.01	7.44	0.00

**Table 4.15:** Degrees of Freedom (DOF) Percentage Matrix for Each Reference Mesh Compared to All Other Meshes.

Reference Target	LE4LE9_B2_4mm	LE4LE9_B3_4mm	LE4B2_4mm	LE4B3_4mm	LE4LE9_B2B3_4mm	LE4B2_2mm	LE4B3_2mm	LE4B2_1mm	LE4B3_1mm	ANSYS_1mm
LE4LE9_B2 (61,440)	0.00	-7.81	-49.23	-10.16	-36.34	-20.31	40.06	326.54	623.83	1800.47
LE4LE9_B3 (56,640)	8.48	0.00	-44.89	-2.54	-30.94	-13.56	51.90	362.74	684.17	2027.26
LE4B2_4mm (31,200)	96.92	81.54	0.00	76.92	25.38	56.92	175.13	740.77	1324.62	3700.77
LE4B3_4mm (55,200)	11.30	2.61	-43.48	0.00	-29.13	-11.30	55.87	374.78	704.42	2080.43
LE4LE9_B2B3 (39,120)	57.06	44.79	-20.26	41.11	0.00	25.16	119.91	569.68	1035.32	2980.37
LE4B2_2mm (48,960)	25.49	15.69	-36.29	12.75	-20.10	0.00	75.77	435.28	807.08	2361.54
LE4B3_2mm (86,040)	-28.60	-34.17	-63.76	-35.86	-54.54	-43.09	0.00	204.61	416.23	1300.93
LE4B2_1mm (262,080)	-76.54	-78.38	-88.12	-78.97	-85.13	-81.31	-67.19	0.00	69.51	359.60
LE4B3_1mm (444,240)	-86.20	-87.29	-93.03	-87.64	-91.24	-88.98	-80.67	-41.01	0.00	171.25
ANSYS_1mm (1,204,560)	-94.90	-95.30	-97.41	-95.42	-96.75	-95.93	-92.86	-78.24	-63.13	0.00

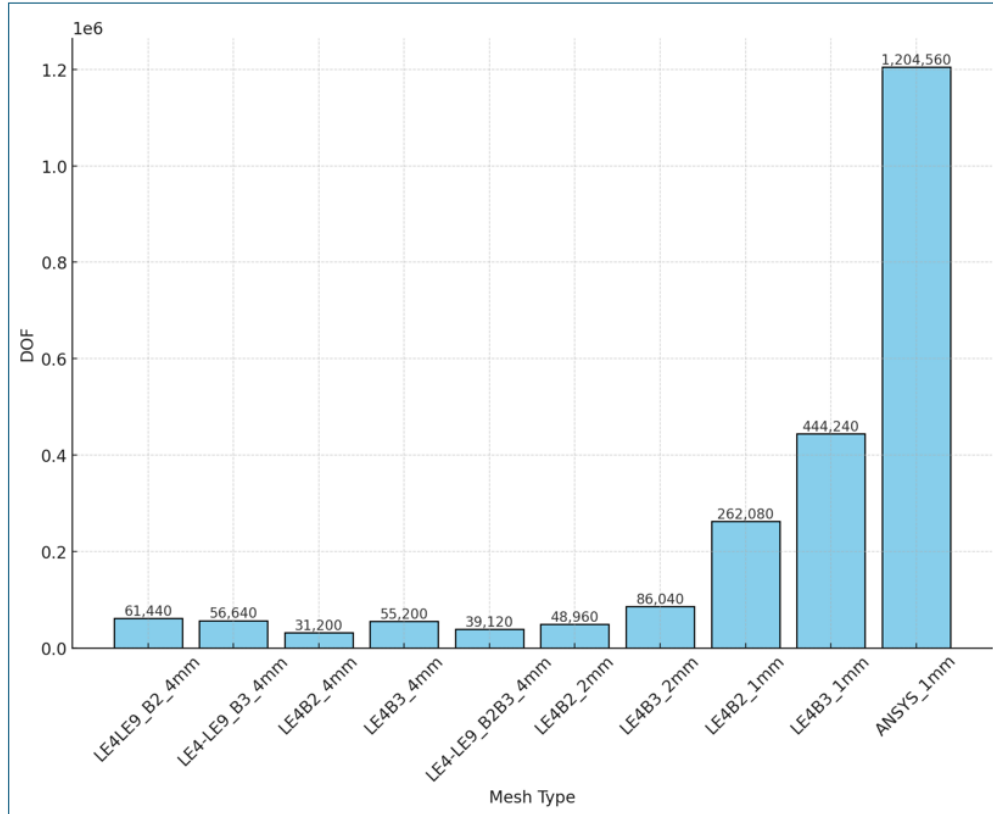


**Figure 4.5:** DOF vs Mesh Type.

## Model Selection for Temperature-Dependent Analysis

From the comparative tables Tab. 4.14 to Tab. 4.15 serving as references in this study, multiple CUF-based finite element (FE) models were tested against a high-fidelity benchmark, **Ansys\_1 mm**, which includes approximately  $1.20 \times 10^6$  degrees of freedom (DOFs). Each CUF-based model employs different polynomial expansions in the thickness direction—B2 for second-order, B3 for third-order— [21] and varies in mesh size (1 mm, 2 mm, or 4 mm). Additionally, some models use a hybrid approach that combines lower- and higher-order elements (e.g., LE4 and LE9) within the same mesh.

A representative subset of the results indicates that third-order expansions (B3) generally yield significantly lower deviations from the reference solution compared to second-order expansions (B2) at the same mesh size. For instance, a B3-based

model with a 4 mm mesh typically shows a modal frequency deviation in the range of 3–4% from the Ansys reference, while a similarly coarse B2-based model can deviate by 8–11%. Although refining the mesh from 4 mm to 1 mm further reduces the deviation—reaching well below 1% in some cases—it also dramatically increases the DOF count.

Hybrid approaches, such as mixing B2 and B3 expansions within the same element framework, can reduce the total DOFs even further. However, in this particular test case, these hybrid solutions exhibit somewhat higher deviations (on the order of 6–7%) compared to uniform B3 models at the same mesh size (which remain closer to 3–4% deviation). Nonetheless, the ability to assign different polynomial orders to specific regions may prove beneficial for more complex or non-uniform geometries.

Among the tested models, LE4 LE9 B3\_4 mm emerges as an especially effective compromise between accuracy and computational cost. It achieves a deviation of around 3–4% from the Ansys benchmark while requiring only about 4–5% of the DOFs used by the reference model. This near-benchmark accuracy and substantial reduction in computational burden make it an excellent candidate for subsequent simulations involving temperature-dependent effects, where thermal gradients, material-property variations, and additional physics would otherwise lead to a significant increase in DOFs.

Although the hybrid (B2B3) approach did not surpass the uniform B3 approach for this specific geometry, its flexibility remains one of the principal advantages of the Carrera Unified Formulation (CUF). Future studies involving more intricate structures or localized high-gradient regions may leverage hybrid expansions more effectively to balance accuracy and computational efficiency.

By selecting LE4 LE9 B3\_4 mm for temperature-dependent analyses, the problem can be approached with confidence that the mesh will provide near-benchmark modal accuracy while leaving sufficient computational resources to incorporate the complexities associated with varying temperature fields.

### 4.3 Temperature-Dependent Modal Analysis Setup

The LE4LE9-B3 formulation identified in the previous section is now applied to three additional temperature conditions— $-30\text{ }^{\circ}\text{C}$ ,  $22\text{ }^{\circ}\text{C}$ , and  $80\text{ }^{\circ}\text{C}$ —beyond the baseline  $40\text{ }^{\circ}\text{C}$  scenario. The finite element mesh, boundary conditions, and solver settings remain unchanged, ensuring a consistent framework for comparing results across all temperatures. However, the material properties (Young’s modulus, Poisson’s ratio, and density) have been adjusted to reflect temperature-dependent changes. By investigating how these modified properties affect the structure’s modal response, the study aims to capture any shifts in natural frequencies and

mode shapes that could be critical for design or operational considerations.

Below in table, Tab. 4.16 are the first ten eigen frequencies (in Hz) obtained from the LE4 LE9-B3 mesh under four different temperature conditions:  $-30^{\circ}\text{C}$ ,  $22^{\circ}\text{C}$ ,  $40^{\circ}\text{C}$ , and  $80^{\circ}\text{C}$ . Each row corresponds to a specific vibrational mode, illustrating how temperature variations influence the structure’s dynamic response.

Mode	$-30^{\circ}\text{C}$	$22^{\circ}\text{C}$	$40^{\circ}\text{C}$	$80^{\circ}\text{C}$
1	551.44	580.04	533.83	530.17
2	701.32	735.91	674.73	675.65
3	1289.71	1317.01	1235.18	1209.08
4	1288.69	1314.32	1266.96	1215.62
5	1451.64	1519.95	1464.24	1391.41
6	1650.50	1736.12	1680.34	1586.46
7	2023.43	2081.34	1979.27	1914.10
8	1980.38	2059.61	1985.77	1898.28
9	2623.34	2691.14	2570.16	2484.37
10	2732.58	2788.47	2725.29	2607.42

**Table 4.16:** Temperature-Dependent Eigen frequencies (in Hz) for the LE4 LE9-B3 Mesh.

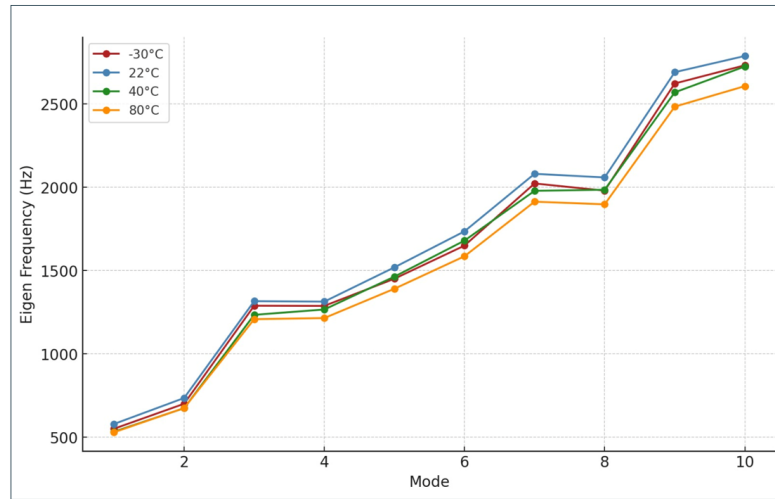


**Figure 4.6:** Temperature-Dependent Eigenfrequencies (in Hz).

The results indicate a clear dependence of the structure’s natural frequencies on temperature. Across the first ten modes,  $22^{\circ}\text{C}$  consistently produces the highest modal frequencies, whereas  $80^{\circ}\text{C}$  yields the lowest. Frequencies at  $-30^{\circ}\text{C}$  and

40 °C lie between these extremes, though the exact ordering can vary slightly by mode.

**Peak Frequencies at 22 °C** Most modes attain their maximum values near room temperature (22 °C). This suggests that, within the tested thermal range, the combined effects of thermal expansion and temperature-sensitive stiffness may create a near-optimal stiffness state at or around room temperature.

**Frequency Reduction at Higher Temperatures** The marked drop in frequency at 80 °C indicates a net softening of the structure. Elevated temperatures typically reduce elastic moduli and increase thermal expansion, both of which can lower overall stiffness and hence natural frequencies.

**Behavior Below Room Temperature** At  $-30$  °C, frequencies remain higher than those at 40 °C or 80 °C but, in most modes, still do not exceed the values at 22 °C. Although one might expect cooler temperatures to increase stiffness, specific temperature-dependent material properties (such as possible phase transitions, non-monotonic modulus variations, or changes in microstructure) could explain why the highest frequencies are found at 22 °C rather than at  $-30$  °C.

**Variations Across Modes** Higher modes exhibit similar trends to the fundamental ones, though the magnitude of the shift can differ from mode to mode. This consistency implies that the underlying thermal effects influence the entire structural domain rather than any single localized region.

**Implications for Design and Operation** Structures subjected to wide temperature swings may experience non-trivial shifts in their dynamic characteristics. The fact that natural frequencies peak at 22 °C and decrease both above and below this temperature highlights the importance of incorporating accurate temperature-dependent material models into modal analyses. Failure to account for these shifts could lead to unexpected resonances or performance issues in real-world applications.

Overall, these results underscore the necessity of performing temperature-dependent modal analyses when designing structures expected to operate in diverse thermal environments. By capturing the interplay between material stiffness changes and thermal expansion, potential resonance conditions can be predicted in desired working ranges to ensure reliable performance across the entire operational temperature spectrum.

## **Methodology for Random Vibration and Fatigue Analysis**

Building on these temperature-dependent modal analysis results, we can further explore the dynamic response and durability of the headlamp components through comprehensive random vibration and fatigue analyses. In the subsequent phases, the operational environment is modeled using a Power Spectral Density (PSD) function defined in accordance with DIN EN60068-2-6 [31], ISO-16750-3 [32], and SAE J1383 [33]. This PSD framework accurately captures the spectrum of vibrational excitations encountered during service, thereby enabling the computation of von Mises stresses on critical components. These stress evaluations form the basis for assessing structural integrity and estimating cumulative fatigue damage. By integrating these analyses with the temperature-dependent modal study, a robust and holistic understanding of both the immediate dynamic behavior and long-term reliability of the headlamp design is achieved, ensuring dependable performance across a diverse range of thermal and vibrational conditions.

### **Random Vibration Analysis**

The PSD is developed using a combination of measured field data and the criteria established in the aforementioned standards, ensuring that the input excitation accurately represents real-world conditions. The analysis employs the modal superposition method whereby each modal Frequency Response Function obtained during the modal analysis is excited by the PSD. By integrating the PSD with these Frequency Response Functions across the relevant frequency range, a comprehensive response spectrum for the headlamp assembly is obtained. Additionally, time domain simulations, such as Monte Carlo methods, are employed to generate representative time histories and to validate the analytical predictions.

After completing the random vibration analysis, the equivalent stress on each component is calculated. These stress results are used to evaluate the structural integrity of the components and to determine whether a component can be expected to have infinite life under the applied loading conditions.

### **Fatigue Analysis**

Building on the vibratory responses derived from the random vibration evaluation, the fatigue analysis estimates the long-term durability of the headlamp components. The dynamic responses at critical locations are converted into stress time histories that capture the cyclic load variations experienced during operation. These stress time histories serve as the basis for calculating cumulative damage, which is used to predict the fatigue life of the components. This cumulative damage assessment

provides valuable insights into whether a component is likely to achieve infinite life or if it may eventually succumb to fatigue damage over time.

This sequential approach from modal analysis through a PSD-based random vibration evaluation in accordance with DIN EN60068-2-6 [31], ISO-16750-3 [32], and SAE J1383 [33], to a detailed fatigue assessment based on equivalent stress and cumulative damage calculations offers a robust framework for understanding both the immediate dynamic behavior and the long-term performance of automotive headlamp components under realistic operational conditions.

## Chapter 5

# Conclusions and Future Perspectives

### Conclusions

This study provides a comprehensive investigation into the modal behavior of automotive headlamps, comparing two distinct modeling approaches: a commercial finite element software and the Carrera Unified Formulation (CUF). The primary aim was to evaluate the accuracy, computational efficiency, and practical applicability of CUF as an alternative to conventional tools widely used in the automotive industry. The findings from this research highlight several critical aspects of CUF's performance in structural vibration analysis.

One of the key outcomes of this study is the confirmation of CUF's accuracy in modal analysis. The comparative results demonstrate that CUF delivers natural frequencies that are in excellent agreement with those obtained from the commercial finite element software, with an average difference of less than 2%. This level of precision underscores CUF's reliability and its ability to match the performance of established commercial platforms. Such accuracy is particularly significant given CUF's additional advantages in computational efficiency and flexibility.

The convergence and mesh refinement study further illustrate CUF's strengths. Through systematic evaluation under varying mesh densities, it was observed that CUF achieves accurate results with significantly fewer degrees of freedom (DOFs) compared to the commercial software. This efficiency is attributed to CUF's capacity to incorporate higher-order elements and advanced kinematic theories, enabling precise modeling even with coarser meshes. The reduction in computational complexity positions CUF as a highly efficient tool for large-scale industrial applications where resource optimization is critical.

Another important aspect explored in this research is CUF's ability to integrate

higher-order elements and advanced kinematic assumptions. The flexibility inherent in CUF allows for the use of various first-order and higher-order elements tailored to specific modeling needs. This adaptability facilitates high-fidelity results with minimal computational effort, making CUF particularly suitable for handling complex geometries and intricate boundary conditions commonly encountered in automotive components. The ability to adjust kinematic formulations further enhances its utility for diverse structural configurations.

The study also delves into the effects of thermal variations on modal behavior, particularly given the presence of plastic components in headlamp assemblies. These materials often operate near their Vicat softening temperatures, necessitating careful consideration of temperature-dependent material properties. By performing modal analyses under three distinct operating temperatures using the best-performing model, this research highlights the critical importance of accounting for thermal effects when analyzing components subjected to real-world operating conditions. Such considerations are essential for ensuring reliable performance under varying thermal environments.

Finally, this investigation validates several anticipated advantages of CUF over traditional finite element methods. Among these, its computational efficiency stands out as a major benefit, as it achieves comparable accuracy with significantly reduced DOFs, thereby minimizing computational time and resource requirements. Additionally, its flexibility in employing higher-order elements and advanced kinematics makes it adaptable to a wide range of structural configurations and loading scenarios. These attributes establish CUF as an effective tool for vibrational analysis in automotive engineering, underscoring its potential for broader adoption in both research and industrial contexts.

In conclusion, this study demonstrates that CUF is not only an accurate but also a computationally efficient alternative to traditional finite element methods for modal analysis. Its ability to deliver high-quality results while reducing computational costs makes it a compelling choice for addressing the challenges associated with structural vibration analysis in automotive applications.

## **Future Perspectives**

The findings of this study open several promising avenues for future research, paving the way for further advancements in the application of the Carrera Unified Formulation (CUF) within automotive engineering. These opportunities span a wide range of topics, each with the potential to enhance the understanding and utility of CUF for structural and vibrational analyses.

A natural progression of this work would involve extending the analysis to random vibration scenarios. By subjecting the headlamp assembly model to real-world excitation spectra representative of operational environments, it would be

possible to investigate its dynamic response under stochastic loading conditions. Such studies would provide critical insights into how the assembly behaves under realistic vibrational loads, offering a more comprehensive understanding of its performance in practical applications.

Another significant area for exploration is the assessment of fatigue behavior. Future research could focus on evaluating equivalent stresses in all three spatial directions for individual components within the headlamp assembly. This approach would enable researchers to predict the lifespan of components under cyclic loading conditions and assess their durability. Such analyses are essential for improving component reliability and ensuring long-term performance under operational stresses.

The inclusion of nonlinear structural analysis represents an exciting opportunity to build upon the findings of this study. Nonlinearities arising from material behavior, such as plasticity, geometric effects like large deformations, or complex boundary conditions could be investigated to better understand their influence on structural performance under extreme conditions. This extension would significantly broaden CUF's applicability by addressing challenges associated with nonlinear dynamic behavior.

While this research focused on headlamp assemblies, the demonstrated success of CUF suggests its potential applicability to other automotive components with complex geometries and loading conditions. Future studies could explore its use in analyzing intricate assemblies such as suspension systems, chassis structures, or powertrain components. Expanding CUF's application across diverse automotive subsystems would further establish its versatility and robustness as a computational tool.

Thermo-mechanical coupling studies also present a valuable direction for future research. Investigating how temperature variations influence both static and dynamic behavior simultaneously could provide critical insights into components subjected to combined thermal and mechanical loads during operation. This line of inquiry is particularly relevant for materials and designs that must withstand fluctuating thermal environments while maintaining structural integrity.

Another promising avenue involves leveraging CUF's computational efficiency for optimization studies aimed at improving component design. By minimizing weight while maintaining or enhancing structural integrity and vibrational performance, optimization efforts could contribute to the development of lighter, more efficient automotive components without compromising safety or functionality. The ability of CUF to handle complex geometries with reduced computational costs makes it an ideal candidate for such studies.

Finally, incorporating advanced material models into CUF-based simulations could significantly enhance its applicability in modern automotive engineering. With the increasing use of composites and other non-conventional materials in

vehicle design, accurate modeling of these materials' behavior is crucial. Future research could focus on integrating these advanced material models into CUF frameworks to enable precise predictions for components made from innovative materials.

In summary, these future research directions underscore the versatility and potential of CUF as a computational tool in automotive engineering. From random vibration analysis and fatigue assessment to nonlinear modeling and optimization studies, each avenue offers unique opportunities to further refine CUF's capabilities and expand its application across a broader spectrum of structural challenges in modern vehicle design.

## **Final Remarks**

This study has successfully demonstrated that CUF is a powerful tool for vibrational analysis of automotive components, offering significant advantages over conventional finite element methods in terms of computational efficiency, flexibility, and accuracy. By achieving high fidelity with reduced computational costs, CUF emerges as a transformative approach capable of addressing complex vibrational challenges faced by modern automotive engineers.

The findings presented here underscore the potential of CUF as a versatile framework for tackling a wide range of structural problems in automotive engineering, from modal analysis to fatigue assessment and beyond.



# Bibliography

- [1] J. Y. Tsao, M. E. Coltrin, M. H. Crawford, and J. A. Simmons. «Solid-State Lighting: An Integrated Human Factors, Technology, and Economic Perspective». In: *Proceedings of the IEEE* 98.7 (2010), pp. 1162–1179 (cit. on pp. 1, 2).
- [2] M. R. Krames et al. «Status and Future of High-Power Light-Emitting Diodes for Solid-State Lighting». In: *Journal of Display Technology* 3.2 (2007), pp. 160–175 (cit. on pp. 1, 2).
- [3] A. Bar-Cohen. *Thermal Management of Microelectronic Equipment*. New York: ASME Press, 2003 (cit. on pp. 2, 3).
- [4] S. Nakamura, S. Pearton, and G. Fasol. *The Blue Laser Diode: The Complete Story*. Berlin: Springer, 2000 (cit. on pp. 2, 3).
- [5] H. J. Hentschel. *Automotive Lighting and Human Vision*. Berlin: Springer, 2007 (cit. on p. 2).
- [6] D. J. Ewins. *Modal Testing: Theory, Practice, and Application*. 2nd. Baldock, UK: Research Studies Press, 2000 (cit. on p. 3).
- [7] S. Suresh. *Fatigue of Materials*. 2nd. Cambridge: Cambridge University Press, 1998 (cit. on p. 3).
- [8] P. R. Boyce. *Human Factors in Lighting*. 3rd. Boca Raton, FL: CRC Press, 2014 (cit. on p. 3).
- [9] C. A. Harper. *Electronic Packaging and Interconnection Handbook*. 4th. New York: McGraw-Hill, 2005 (cit. on p. 3).
- [10] *ISO 16750: Road Vehicles—Environmental Conditions and Testing for Electrical and Electronic Equipment*. Geneva: International Organization for Standardization, 2012 (cit. on pp. 3, 4).
- [11] O. C. Zienkiewicz, R. L. Taylor, and J. Z. Zhu. *The Finite Element Method: Its Basis and Fundamentals*. 7th. Oxford: Elsevier, 2013 (cit. on p. 3).
- [12] G. Pahl, W. Beitz, J. Feldhusen, and K.-H. Grote. *Engineering Design: A Systematic Approach*. 3rd. London: Springer, 2007 (cit. on p. 4).

- [13] *VW80000: Testing of Electrical and Electronic Components in Motor Vehicles*. Wolfsburg, Germany: Volkswagen AG, 2015 (cit. on p. 4).
- [14] R. W. Hertzberg, J. A. Manson, and M. D. Skibo. *Fatigue of Engineering Plastics*. New York: Academic Press, 1980 (cit. on p. 4).
- [15] *ECE Regulation No. 48: Uniform Provisions Concerning the Approval of Vehicles with Regard to the Installation of Lighting and Light-Signalling Devices*. Geneva, Switzerland: United Nations Economic Commission for Europe, 2020 (cit. on p. 4).
- [16] *ECE Regulation No. 112: Advanced Lighting Systems for Vehicles*. Geneva, Switzerland: United Nations Economic Commission for Europe, 2020 (cit. on p. 4).
- [17] *FMVSS No. 108: Lamps, Reflective Devices, and Associated Equipment*. Washington, D.C., USA: National Highway Traffic Safety Administration, 2020 (cit. on p. 4).
- [18] *SAE J551: Dynamic and Fatigue Testing for Headlamp Components*. Warrendale, PA, USA: Society of Automotive Engineers, 2019 (cit. on p. 4).
- [19] E. Carrera. «Theories and finite elements for multilayered, anisotropic, composite plates and shells». In: *Archives of Computational Methods in Engineering* 9.2 (2002), pp. 87–140 (cit. on pp. 7, 17, 20).
- [20] E. Carrera. «Historical review of Zig-Zag theories for multilayered plates and shells». In: *Applied Mechanics Reviews* 56.3 (2003), pp. 287–308 (cit. on pp. 7, 8, 14, 17).
- [21] E. Carrera, M. Cinefra, M. Petrolo, and E. Zappino. *Finite Element Analysis of Structures Through Unified Formulation*. John Wiley & Sons, 2014 (cit. on pp. 7, 9–12, 16, 17, 20, 54).
- [22] Alfonso Pagani. «Component-wise models for static, dynamic and aeroelastic analyses of metallic and composite aerospace structures». PhD thesis. Politecnico di Torino, 2015 (cit. on pp. 7, 9, 12, 13, 15, 17).
- [23] P. F. Pai. *Highly Flexible Structures: Modeling, Computation, and Experimentation*. Springer, 2007 (cit. on pp. 8, 19, 20).
- [24] Rodolfo Azzara. «Nonlinear and Linearized Analysis of Vibrations of Loaded Anisotropic Beam/Plate/Shell Structures». PhD thesis. Politecnico di Torino, 2023 (cit. on pp. 9, 16, 20).
- [25] E. Carrera and S. Brischetto. «Analysis of Thickness Locking in Classical, Refined, and Mixed Multilayered Plate Theories». In: *Composite Structures* 82.4 (2008), pp. 549–562 (cit. on pp. 13, 19).

- [26] Manish Hassan Nagaraj. «Higher-order layer-wise models for the progressive damage and impact analysis of composite structures». PhD thesis. Politecnico di Torino, 2021 (cit. on pp. 13, 19).
- [27] Riccardo Augello. «Advanced FEs for the micropolar and geometrical nonlinear analyses of composite structures». PhD thesis. Politecnico di Torino, 2021 (cit. on pp. 14, 19).
- [28] Amedeo Grasso. «Implementation of classical and advanced failure criteria for composite layered structures in FEMAP and assessment of results». MA thesis. Politecnico di Torino, 2018 (cit. on pp. 15, 19).
- [29] F. Zhu, R. Augello, R. Azzara, A. Pagani, E. Carrera, and W. Chen. «Vibration Analysis of Curved Panel Subjected to Internal Pressure and Axial Compression». In: *AIAA Journal* 60.12 (2022), pp. 6842–6853 (cit. on pp. 18, 20).
- [30] K. Foroutan, H. Ahmadi, and E. Carrera. «Free vibration analysis of a sandwich cylindrical shell with an FG core based on the CUF». In: *Smart Structures and Systems* 30.2 (2022), pp. 121–133 (cit. on p. 20).
- [31] *DIN EN 60068-2-6: Environmental Testing – Part 2-6: Tests – Test Fc: Vibration (sinusoidal)*. Berlin, Germany: Deutsches Institut für Normung, 2001 (cit. on pp. 58, 59).
- [32] *ISO 16750-3: Road Vehicles – Environmental Conditions and Testing for Electrical and Electronic Equipment – Part 3: Mechanical Loads*. Geneva: International Organization for Standardization, 2012 (cit. on pp. 58, 59).
- [33] *SAE J1383: Vibration Testing of Automotive Components*. Warrendale, PA, USA: Society of Automotive Engineers, 1995 (cit. on pp. 58, 59).